On the effectiveness of Reynolds-averaged and subgrid scale models in predicting flows inside car cabins

Grossi, Giorgio; Arpino, Fausto; Bertone, Michele; Cortellessa, Gino; Sciacchitano, Andrea

DOI
10.1063/5.0180823

Publication date
2024

Document Version
Final published version

Published in
Physics of Fluids

Physics of Fluids

RESEARCH ARTICLE | JANUARY 22 2024

On the effectiveness of Reynolds-averaged and subgrid scale models in predicting flows inside car cabins

Giorgio Grossi ; Fausto Arpino ; Michele Bertone ; Gino Cortellessa ; Andrea Sciacchitano

Physics of Fluids 36, 015137 (2024)
https://doi.org/10.1063/5.0180823

Physics of Fluids ARTICLE pubs.aip.org/aip/pof

On the effectiveness of Reynolds-averaged and subgrid scale models in predicting flows inside car cabins

Cite as: Phys. Fluids **36**, 015137 (2024); doi: 10.1063/5.0180823
Submitted: 12 October 2023 · Accepted: 26 December 2023 ·
Published Online: 22 January 2024

Giorgio Grossi,[1,a)] Fausto Arpino,[1] Michele Bertone,[1] Gino Cortellessa,[1] and Andrea Sciacchitano[2]

AFFILIATIONS

[1]Department of Civil and Mechanical Engineering, Università degli Studi di Cassino e del Lazio Meridionale, via G. Di Biasio 43, Cassino, Italy

[2]Aerospace Engineering Department, Delft University of Technology, Kluyverweg 1, 2629 HS Delft, The Netherlands

[a)]**Author to whom correspondence should be addressed:** giorgio.grossi@unicas.it

ABSTRACT

The aim of the present study is to analyze the performances of unsteady Reynolds-averaged Navier–Stokes (URANS) and large eddy simulation (LES) approaches in predicting the airflow patterns inside car cabins and to give insight in the design of computational fluid dynamics simulations of a real car cabin. For this purpose, one eddy viscosity-based turbulence model (shear stress transport k–ω) and two subgrid scale models (wall-adapting local eddy-viscosity and dynamic kinetic energy) were tested, and numerical results were compared with particle image velocimetry measurements carried out on a commercial car. The URANS model exhibited great accuracy in predicting the mean flow behavior and was appreciably outperformed by the LES models only far from the inlet sections. For this reason, it was deemed suitable for conducting further analyses, aimed at characterizing the airflow patterns in winter and summer conditions and performing a thermal comfort analysis. The thermal regime was found to have a very little effect on the air flow patterns, once the quasi-steady state regime is achieved; in fact, both in winter and in summer, the temperature field is fairly uniform within the car cabin, making the contribution of buoyancy negligible and velocity fields to be very similar in the two seasons. Findings also reveal that thermal comfort sensation can be different for passengers sharing the same car but sitting on different seats; this aspect should be considered when designing and operating the ventilation system, since the minimum comfort requirements should be met for all the occupants.

I. INTRODUCTION

Computational fluid dynamics (CFD) has undergone significant developments in the last few years, becoming a suitable tool for investigating velocity, pressure, and temperature fields in various indoor microenvironments, including aircraft cabins,[1–17] trains,[18–20] buses,[21–28] and cars.[29–45] Despite its versatility, if not properly validated, numerical modeling may be affected by large errors and produce misleading results, thereby eliminating all the advantages deriving by its employment (i.e., reduced costs and times with respect to experiments). These errors could be induced by several factors: definition and discretization of the domain (oversimplification of the geometry and bad quality cells in the computational grid), selection of the boundary conditions, and wrong assumptions in the mathematical modeling (i.e., choice of the governing equations to be solved and models for the fluid and solid properties). Therefore, before applying any numerical tool to engineering problems, a verification and validation procedure is required to ensure the reliability and accuracy of the results.[46] In this regard, the particle image velocimetry (PIV) technique can be used to provide accurate data for the validation of numerical simulations. Looking at the scientific literature, several studies rely on PIV data for the validation of numerical codes. Among others, You *et al.*[2,9] employed PIV data to validate the CFD models adopted to investigate the impact of gaspers on the airflow patterns inside an aircraft cabin; Yang *et al.*[4] conducted large eddy simulations to investigate the airflow characteristics in a simplified Boeing 737-200 cabin model, validating numerical results against PIV measurements. While a considerable amount of research was dedicated to achieving a better understanding of airflow patterns inside aircraft, buses, and trains, very few properly validated numerical studies are available concerning car cabins. Chang *et al.*[31] developed a CFD model to study the effects of the ventilation rate on the air quality inside a car cabin and to establish the amount of fresh air required for each occupant in a vehicle; however, validation of the

numerical model is provided by comparing simulated and experimental CO_2 concentrations in the cabin and not in terms of velocity fields. Khatoon and Kim[33] and Yang *et al.*[32] performed CFD simulations to investigate passenger comfort inside car cabins; even in these cases, validation was not provided in terms of velocity fields but comparing temperature values at specific points of the domain. Zhang *et al.*[34,35] evaluated the influence of different factors on the thermal comfort and the energy consumption in a car cabin, comparing measured and predicted transient temperatures. Dehne *et al.*[36] presented three vertical ventilation concepts for car cabins, comparing them to common dashboard ventilation using both experimental and numerical approaches; the analyses were carried out on a simplified cabin prototype and the CFD model was validated with mean temperature and velocity values taken at multiple points of the cabin. Ullrich *et al.*[37] conducted a numerical study, validated with PIV measurements, in order to optimize the heating, ventilation, and air conditioning (HVAC) system and reduce its energy consumption; unfortunately, detailed information about the geometry is not available, making the reproduction of the numerical setup not possible. Danca *et al.*[41,42] carried out experimental and numerical analyses to investigate the air distribution and the thermal comfort inside a car cabin mockup; a simplified geometry was used to reproduce the in-vehicle environment, which may be not representative of life-like scenarios.

Mathai *et al.*[39] performed Reynolds-averaged Navier–Stokes (RANS) simulations to study the aerosol distribution inside a vehicle cabin, for different combinations of open and closed windows; Sen and Singh[40] also used a CFD model to analyze the droplets dispersion inside a moving car with the windows open, by adopting a Eulerian–Lagrangian approach. Both these studies, however, make use of an extremely simplified geometry and do not provide a quantitative validation of the numerical results.

More recently, Sip *et al.*[47] provided a benchmark for the characterization of the flow immediately downstream of automotive vents, comparing two theoretical approaches and validating them with measurements acquired with the constant temperature anemometry (CTA) technique. Finally, Djeddou *et al.*[38] analyzed the performances of five RANS turbulence models in predicting the airflow inside a passenger car cabin, providing validation against mean velocities and turbulence intensity profiles obtained with hot-wire anemometers; as claimed by the authors themselves, the PIV technique would have been more suitable since it is non-intrusive and provides information about the direction of the flow.

In previous research activities,[29,30] the authors realized a transient, non-isothermal numerical model able to predict airborne droplet dispersion inside car cabins; the tool was validated against PIV measurements carried out on a glass-made scaled model and then applied to quantify the risk of infection from SARS-CoV-2 of passengers sharing a car with an infected subject for a 30 min journey. Findings revealed that CFD approaches are needed to properly describe the airflow patterns in such confined spaces and can be used to design new ventilation strategies for the purpose of improving the indoor air quality (IAQ) and the comfort of the occupants. The results obtained by CFD analyses, however, may be considerably influenced by the geometry adopted for reproducing the in-vehicle environment; hence, a situation as realistic as possible is desirable. For this reason, on the wave of our previous works, transient non-isothermal CFD simulations are herein performed and compared with PIV measurements carried out on a commercial car. Both unsteady RANS (URANS) and large eddy simulation (LES) approaches are employed, assessing the performance of one eddy viscosity-based model, the shear stress transport (SST) k–ω and two subgrid scale (SGS) models, the wall-adapting local eddy-viscosity (WALE), and the dynamic kinetic energy (KE) models.

The URANS model, owing to the very good agreement with the experimental results and to the reduced computational time with respect to LES, was selected to conduct further numerical analyses, aimed at characterizing the thermal-fluid dynamics fields inside the car cabin in summer and winter conditions. A thermal comfort analysis is also conducted, calculating the evolution over time of the predicted mean vote (PMV) and the predicted percentage dissatisfied (PPD)[48,49] at multiple significant points of the cabin. For the scenarios here presented, the car cabin is assumed to be empty, since the PIV measurements were carried out in the absence of occupants. The main objective of the present work is, in fact, to numerically reproduce the experiments and to give insight in the design of CFD simulations of a real car cabin (from the creation of the geometry model to the selection of the boundary conditions and of the most convenient approach for turbulence modeling). The focus is also on the comparison between URANS and LES approaches, particularly useful in the modern scientific landscape. The increasing computational resources available to researchers and industries worldwide are, indeed, expanding the use of LES in pursuit of more accurate and reliable results. However, this comes with higher complexity and computational costs, making it necessary to define when such complications are required.

Future works, relying on the numerical tool here validated, will include the presence of the occupants and explore broader scenarios, with the purpose of improving the indoor air quality (IAQ) and the comfort of the passengers as well as reducing the energy consumption by the car HVAC system.

The paper is organized as follows: Sec. II outlines the methodology, the experimental setup, and the case study; details on the numerical setup are provided in Sec. III; Sec. IV shows the comparison of URANS and LES results with PIV data; in Sec. V, the discussion of numerically predicted velocity and temperature fields in winter and summer conditions is provided, together with a thermal comfort analysis; finally, conclusions are drawn in Sec. VI of the paper.

II. METHODOLOGY

The HVAC system produces a highly transient, three-dimensional, and turbulent flow pattern inside the car cabin, which is influenced by several factors: position and shape of the vents, inlet air velocity, geometry, and size of the interior.[29,30,50] A careful design of the numerical analyses is, thus, required; in the present study, particular attention was paid to the reproduction of the in-vehicle environment, identification of inlet and outlet sections, and the proper definition of the boundary conditions.

The experimental facility is represented by a Peugeot 206, shown in Fig. 1. Highlighted in the left picture are the vents enabled during the experiments (representing the front ventilation mode). On the right, the position of the axis system selected as the reference for PIV measurements is shown; it has been placed in the middle of the central vents to ensure the repeatability of the experimental conditions.

PIV measurements, and so the numerical simulations, were carried out for the case of front ventilation mode, fresh air intake (i.e., no air recirculation), and HVAC system's fan strength set at level 3 out of the four available for mass flow rate adjustments.

FIG. 1. The experimental facility. Left: picture of the car dashboard, with the front vents highlighted; right: position of the axis system selected as reference for PIV measurements.

A. PIV experimental setup

Experiments were conducted in the backyard of the Aerodynamics Laboratories of the Delft University of Technology; for security reasons, the car and all the equipment employed were placed inside a tent 3 m wide, 2.6 m high, and 6 m long. Temperature and humidity inside and outside the car (i.e., inside the tent) were monitored during the experiments with an Alecto Weather Station 1500, ensuring a resolution uncertainty of 0.1 K for temperature and 1% for relative humidity.

Planar PIV measurements were taken on the xy plane at $z = -0.03$ m (with reference to the axis system shown in Fig. 1). Two cameras were used to have a wider area for the acquisition of velocity fields, able to capture the tail of the jet coming out of the central vents. The measuring area is displayed in the right image of Fig. 2, whereas on the left the arrangement of cameras and laser is sketched.

The laser sheet gains access to the cabin through the windshield and enlightens the flow field, seeded with micrometric water-glycol droplets produced by a SAFEX seeding generator placed inside the car cabin; the optical access is provided to the cameras, placed on the right of the car, by the side windows (which were kept closed during the tests). A set of 500 uncorrelated image pairs was recorded for each camera; in the overlap area, the arithmetic average of the acquired flow fields was computed.

The parameters of the experiments are reported in Table I. For further details, the reader is referred to our recently published work,[51] presenting the preliminary results of an extensive experimental campaign carried out on the same car here numerically reproduced.

B. Geometry modeling

To facilitate the analyses and save computational resources, a simplified model of the Peugeot 206 car has been reproduced while keeping the main geometric characteristics of the passenger compartment; in fact, an overly detailed geometry would require an excessive grid refinement with unreasonable CPU times, which is beyond the scope of the present work. The cabin, whose internal volume is 2.05 m^3, has four inlet vents (two in the center and one at each side; only these vents have been considered for the computational domain definition, since in the experimental campaign only the front ventilation mode has been investigated) and one outlet section as shown in Fig. 3. Specific analyses were conducted to identify the output: the flow induced by the ventilation system was seeded with micrometric water-glycol droplets produced by a SAFEX seeding generator (the same used for PIV measurements, see Table I), observing the flow patterns within the cabin and visually detecting where the air leaves the passenger compartment; these investigations revealed that the air exits the cabin at multiple locations, being the vehicle not perfectly air-tight, but the main flow is directed back to the parcel shelf; this last finding was later confirmed by PIV measurements, described with a greater detail in Ref. 51, and for these reasons, the exit section has been defined as depicted in Fig. 3. To reproduce the inlet vents, only the section

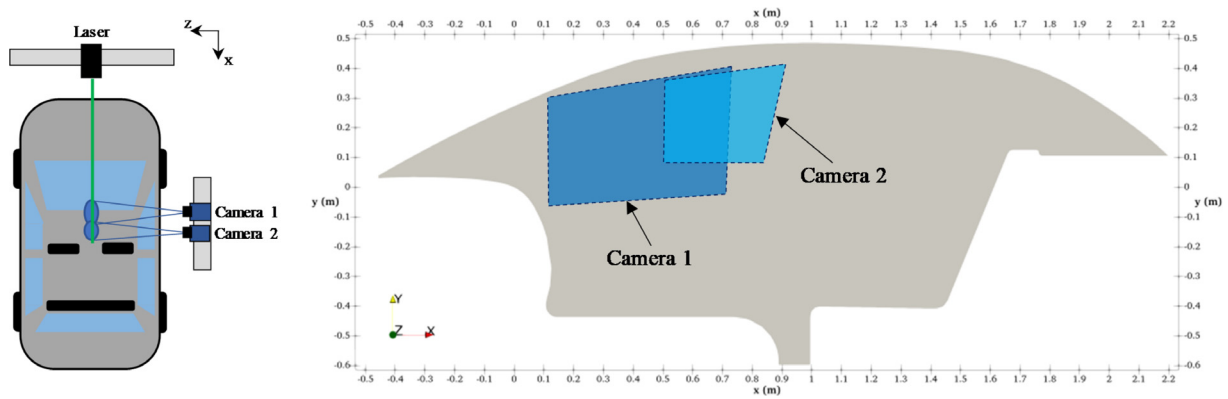

FIG. 2. Sketch of the PIV measurements setup. Left: arrangement of cameras and laser; right: measuring area covered by the cameras.

TABLE I. Experimental parameters.

Parameter	Camera 1	Camera 2
Illumination	Quantel Evergreen Nd:YAG laser (200 mJ pulse energy, wavelength $\lambda = 532$ nm, maximum repetition frequency of 15 Hz)	
Seeding system	SAFEX seeding generator (water-glycol droplets of 1 μm median diameter)	
Imaging	LaVision Imager *sCMOS* camera (16 bit, 2560 × 2160 pixels, 6.5 μm pixel size)	
f-number, f#	5.6	4
Lens objective (mm)	35	50
Field of view (mm^2)	653 × 545	454 × 382
Magnification factor	0.025	0.037
Acquisition frequency (Hz)	15	
Pulse separation, Δt (ms)	1	
Number of recordings	500	
Outside temperature (°C)	30.2	
Relative humidity (%)	28	
Inside temperature (°C)	43.6	

available to the air flow stream has been considered. For what concerns the walls, glazed surfaces (i.e., windshield, side windows, and rear window) have been distinguished from non-glazed ones to ensure an accurate definition of the boundary conditions.

C. Definition of the inlet mean velocity boundary condition

Being the air flow patterns within the car cabin strongly affected by the velocity at the inlet sections, a proper definition of such boundary condition is desirable to ensure a trustable reproduction of actual operating conditions. For this purpose, 3D measurements of the airflow exiting the front vents were performed by using the ProCap Compact 5-hole digital probe by Streamwise; a detailed description of the experimental apparatus is available in Ref. 51 to which the interested reader is referred. The measured mean velocity data were fitted with the 2D Gaussian function represented by Eq. (1), employing the Excel Evolutionary solver. Gaussian fitting for velocity profile at the inlet allows us to have a simplified expression, which can be implemented with more ease as the boundary condition in the code

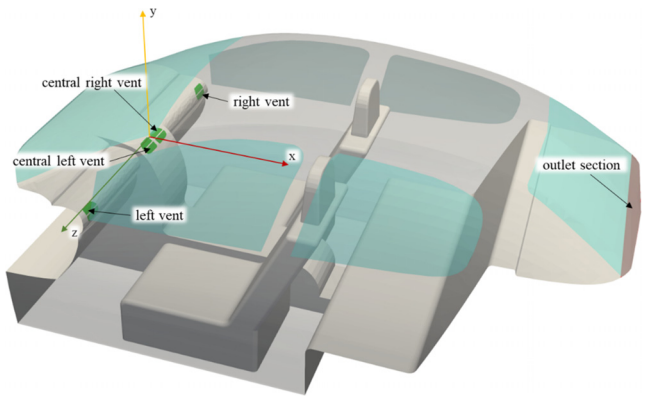

FIG. 3. Computational domain with boundary patches.

$$u_G(y,z) = u_{\max} \cdot \exp\left(-\left(\frac{(z-z_0)^2}{2{\sigma_z}^2} + \frac{(y-y_0)^2}{2{\sigma_y}^2}\right)\right). \quad (1)$$

The parameters of the Gaussian function implemented in the numerical simulations are listed in Table II for the different boundary patches, whereas in Fig. 4, a visual comparison among measured and numerically reproduced velocity fields is provided. The asymmetry of the HVAC system has been reproduced in order to have an accurate reproduction of the thermal-fluid dynamics fields inside the car cabin. The experimental fields of Fig. 4 are taken on surfaces whose normal vector lies in the xy plane and is inclined to the y axis by 73° for central vents and 60° for lateral vents.

D. Case study

The main objective of this work is to assess the accuracy of URANS and LES approaches in predicting the characteristics of flow patterns arising inside car cabins and to point out the main criticalities that may affect the CFD modeling of these indoor microenvironments. This is achieved through a careful analysis of all numerical aspects (Sec. III) and a comparison with PIV measurements (extensively described in Sec. IV).

The URANS model is then employed to study the airflow characteristics in winter and summer conditions, bringing up the main

TABLE II. Parameters for the Gaussian function imposing the mean velocity magnitude at the inlet.

Surface	$u_{\max}$ (m/s)	z_0 (m)	y_0 (m)	σ_z (m)	σ_y (m)
Central right vent	4.900	−0.052 61	−0.012 22	0.0244	0.0106
Central left vent	4.240	0.052 61	−0.012 22	0.0244	0.0106
Right vent	4.520	−0.578 65	−0.041 92	0.0244	0.0159
Left vent	3.675	0.578 65	−0.041 92	0.0244	0.0159

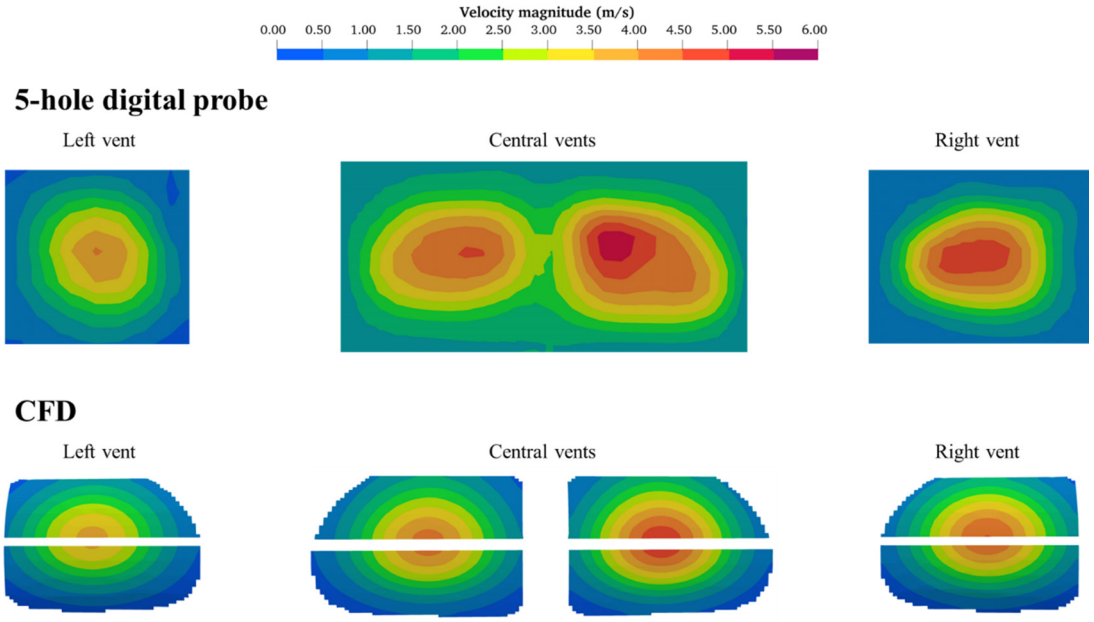

FIG. 4. Measured (top) and numerically reproduced (bottom) mean velocity fields at the inlet vents, in the case of HVAC system's fan strength set at level 3.

aspects affecting the well-being of the passengers. The following reference temperatures have been assumed: for winter scenario, the internal temperature is set to 20 °C and the external to 10 °C; for summer scenario, internal and external temperatures are 25 and 30 °C, respectively. Such outdoor temperature values were selected as representative of the typical Mediterranean climate, as claimed by Golasi *et al.*[52]

E. Methodology for thermal comfort assessment

Despite the existence of more advanced methods for thermal comfort predictions,[53–56] in our analysis, the PMV and PPD indices (recommended by the international standards[48,49,57]) are selected as reference parameters, due to the relatively easy implementation and to the easy-to-grasp information provided about the well-being of the passengers. Their usage to assess thermal comfort in transient environments is allowed if the operative temperature does not change more than ∼2 °C during a 1 h period;[48,49] however, if these temperature variations are induced by adjustments by the users (as in the scenarios here investigated), higher values may be acceptable.[49]

The PMV and PPD indices have been calculated according to the ISO 7730 Standard,[48] and their evolution over time has been monitored in correspondence of five points inside the domain, as explained in Sec. V; for this purpose, the *pythermalcomfort* package developed by Tartarini and Schiavon[58] was employed.

The PMV is an index allowing us to predict the mean value of votes of a large group of people exposed to same environment on the seven-point thermal sensation scale given in Table III, based on the heat balance of the human body.

The PMV can be calculated using the following equations:

$$\begin{aligned}\mathrm{PMV} = {} & \left[0.303 \cdot \exp(-0.036 \cdot M) + 0.028\right] \\ & \cdot \left\{(M - W) - 3.05 \cdot 10^{-3}\right. \\ & \cdot \left[5733 - 6.99 \cdot (M - W) - p_a\right] - 0.42 \\ & \cdot \left[(M - W) - 58.15\right] - 1.7 \cdot 10^{-5} \cdot M \\ & \cdot (5867 - p_a) - 0.0014 \cdot M \cdot (34 - t_a) \\ & - 3.96 \cdot 10^{-8} \cdot f_{\mathrm{cl}} \cdot \left[(t_{cl} + 273)^4 - (\bar{t}_r + 273)^4\right] \\ & \left. - f_{\mathrm{cl}} \cdot h_c \cdot (t_{\mathrm{cl}} - t_a)\right\}, \end{aligned} \tag{2}$$

$$\begin{aligned} t_{\mathrm{cl}} = {} & 35.7 - 0.028 \cdot (M - W) - I_{\mathrm{cl}} \\ & \cdot \left\{3.96 \cdot 10^{-8} \cdot f_{\mathrm{cl}} \cdot \left[(t_{\mathrm{cl}} + 273)^4 - (\bar{t}_r + 273)^4\right]\right. \\ & \left. + f_{\mathrm{cl}} \cdot h_c \cdot (t_{\mathrm{cl}} - t_a)\right\}, \end{aligned} \tag{3}$$

$$h_c = \begin{cases} 2.38 \cdot |t_{\mathrm{cl}} - t_a|^{0.25}, & 2.38 \cdot |t_{\mathrm{cl}} - t_a|^{0.25} > 12.1 \cdot \sqrt{v_{\mathrm{ar}}} \\ 12.1 \cdot \sqrt{v_{\mathrm{ar}}}, & 2.38 \cdot |t_{\mathrm{cl}} - t_a|^{0.25} < 12.1 \cdot \sqrt{v_{\mathrm{ar}}} \end{cases}, \tag{4}$$

$$v_{\mathrm{ar}} = v + v_{\mathrm{ag}}, \tag{5}$$

TABLE III. Seven-point thermal sensation scale.

+3	Hot
+2	Warm
+1	Slightly warm
0	Neutral
−1	Slightly cool
−2	Cool
−3	Cold

$$v_{ag} = \begin{cases} 0, & M \leq 58.2\ W/m^2 \\ 0.3 \cdot \left(\frac{M}{58.2} - 1\right), & M > 58.2\ W/m^2, \end{cases} \quad (6)$$

$$f_{cl} = \begin{cases} 1.00 + 1.290 I_{cl}, & I_{cl} \leq 0.078\ m^2 \cdot K/W, \\ 1.05 + 0.645 I_{cl}, & I_{cl} > 0.078\ m^2 \cdot K/W, \end{cases} \quad (7)$$

where M is the metabolic rate (W/m^2), W is the effective mechanical power (W/m^2), I_{cl} is the clothing insulation (m^2 K/W), f_{cl} is the clothing surface area factor, t_a is the air temperature (°C), $\bar{t}_r$ is the mean radiant temperature (°C), v_{ar} is the relative air velocity combining the average air speed of the environment v plus the relative air speed resulting from the body movement v_{ag} (m/s), p_a is the water vapor partial pressure (Pa), h_c is the convective heat transfer coefficient [W/(m^2 K)], and t_{cl} is the clothing surface temperature.

On the other hand, the PPD predicts the percentage of thermally dissatisfied people who feel too cool or too warm. According to the ISO 7730 Standard, thermally dissatisfied people are those who will vote hot, warm, cool, or cold on the seven-point thermal sensation scale of Table III; the rest of the group will feel thermally neutral, slightly warm, or slightly cool. With the PMV value determined, the PPD is calculated using the following equation:

$$PPD = 100 - 95 \cdot \exp(-0.033\,53 \cdot PMV^4 - 0.2179 \cdot PMV^2). \quad (8)$$

An environment satisfying all the occupants is not possible due to the individual thermal sensation; for this reason, standards specify particular criteria to be met.[59] The ISO 7730 defines three classes: (i) class A, requiring $-0.2 < PMV < 0.2$ (PPD $< 6\%$), represents a high level of expectation and is intended for spaces occupied by very sensitive and fragile persons with particular requirements; (ii) class B, with $-0.5 < PMV < 0.5$ (PPD $< 10\%$), is the level commonly adopted for design and operation; and (iii) class C, with $-0.7 < PMV < 0.7$ (PPD $< 15\%$), which ensures an environment that is still considered acceptable but presents some risk of reduced occupants performance.[59] In the present study, the class B is taken as a reference, since this is the same level defined as acceptable by the American national standard ASHRAE 55-2020.[49]

III. NUMERICAL SETUP

URANS and LES simulations were performed employing the open-source OpenFOAM code, based on the finite volume formulation. Air density is assumed to vary linearly with temperature, according to the Boussinesq approximation, due to the small temperature gradients in the computational domain.[60]

A. Setup for URANS simulations

For URANS simulations, the shear stress transport (SST) k–ω model was selected since previous studies on a simplified car cabin revealed its better performance with respect to other eddy viscosity-based models.[29] Transient simulations were carried out using the PIMPLE algorithm, which is a combination of PISO (pressure-implicit with splitting of operators) and SIMPLE (semi-implicit method for pressure-linked equations), processing the overall transient phenomenon as consecutive steady-state time steps; a time step of 0.01 s was adopted and as requirement for time step convergence the scaled residuals were set $<10^{-3}$ for pressure and $<10^{-5}$ for velocity.

To ensure the independence of the URANS solution from the adopted grid, a mesh sensitivity analysis has been performed. Three unstructured hex-dominant meshes have been employed, generated using the *snappyHexMesh* algorithm. An x–y plane at $z = 0$ [see Fig. 5(a)] is available in Figs. 5(b)–5(d) for the different grids, while details of the computational meshes are summarized in Table IV.

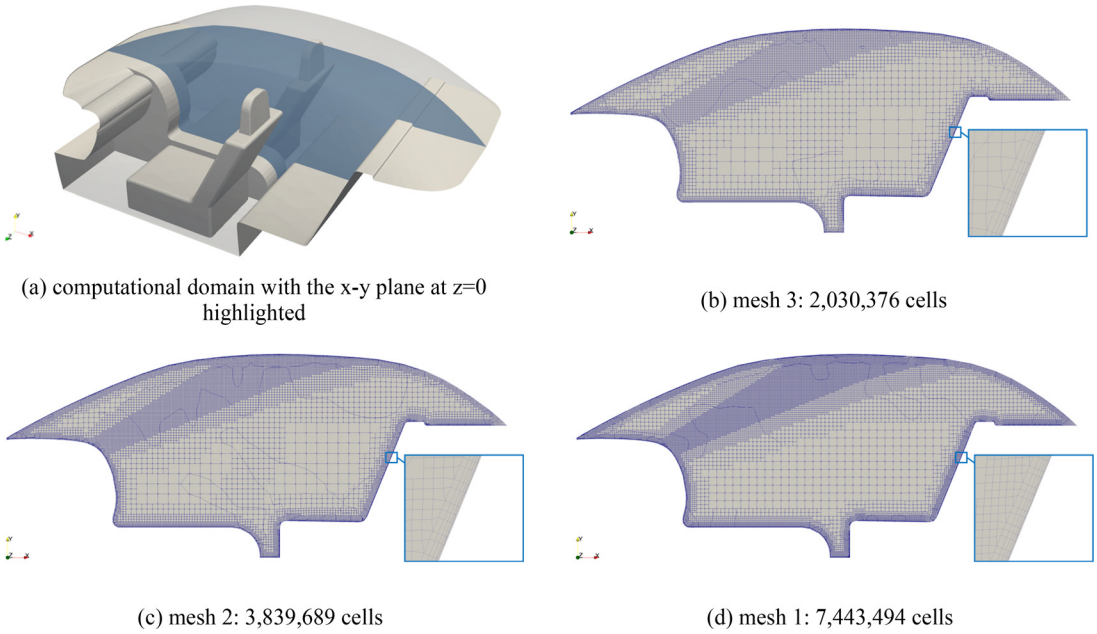

(a) computational domain with the x-y plane at z=0 highlighted

(b) mesh 3: 2,030,376 cells

(c) mesh 2: 3,839,689 cells

(d) mesh 1: 7,443,494 cells

FIG. 5. Computational domain with the x–y plane at $z = 0$ highlighted (a); slices at $z = 0$ of the computational grids employed for mesh sensitivity analysis [(b)–(d)].

TABLE IV. Details of the computational meshes.

Mesh no.	Number of cells	Skewness max	Non orthogonality max	y^+ max	y^+ min	y^+ avg
3	2 030 376	4.52	50	25.94	5.78×10^{-04}	1.45
2	3 839 689	4.77	65	24.19	3.46×10^{-04}	1.31
1	7 443 494	3.56	65	19.32	2.84×10^{-04}	1.28

All grids were refined in the jet zone (upper area of the passenger compartment) and in correspondence of solid walls, where a boundary layer region composed of five layers has been defined; this construction strategy allowed accurate description of the gradients of the solution and led to the maximum, minimum, and average $y+$ values reported in Table IV. Grid convergence tests were performed considering the Richardson error estimation procedure.[61] According to such criterion, the average error in a fine grid solution and in a coarse grid solution is determined by

$$E^{\text{fine}}_{\text{Mesh1}} = \frac{f_2 - f_1}{1 - r^p}, \tag{9}$$

$$E^{\text{coarse}}_{\text{Mesh2}} = \frac{r^p (f_2 - f_1)}{1 - r^p}, \tag{10}$$

where p is the formal order of accuracy of the algorithm, calculated as follows:

$$p = \frac{\ln\left(\frac{f_3 - f_2}{f_2 - f_1}\right)}{\ln(r)}. \tag{11}$$

In the expressions above f_1, f_2, and f_3 are numerical solutions obtained with grid spacing equal to h_1, h_2, and h_3, respectively (with subscript 1 indicating the finest grid in the present notation) and $r = h_i/h_{i-1} > 1$ is the refinement factor adopted for the generation of the different grids. A constant refinement factor equal to 1.3 was adopted here, and the average formal order of accuracy of the algorithm is equal to 3.36. Figure 6 shows the velocity profiles compared for the sensitivity analysis, obtained with the three selected grids at $x = 0.25$ and $z = -0.03$ m (i.e., the measuring plane of the PIV experiment). The location where the profiles are extracted is highlighted in yellow color on the right picture in Fig. 6, portraying the above-mentioned x–y plane at $z = -0.03$ m. The average error obtained for Mesh 2, $E^{\text{coarse}}_{\text{Mesh2}}$, is equal to 4.03% while the average error obtained for Mesh 1 $E^{\text{fine}}_{\text{Mesh1}}$ is equal to 2.85%. Being the error below the 5%, it can be concluded that Mesh 2 provides nearly grid-independent results and has been selected for numerical investigations.

Since the flow field is affected by periodic temporal fluctuations in the jet region, grid convergence study and numerical vs experimental comparison were conducted in terms of time-averaged velocity fields. Targeted analyses were conducted to establish the proper averaging time interval, finding that 25 s are needed to have a deviation of less than 1% among the predicted mean velocity profiles.

B. Setup for large-eddy simulations

The LES simulations were initialized with the results from the URANS simulation and carried out on the finest grid (i.e., Mesh 1). Pressure–velocity coupling was solved with the PISO algorithm, setting the maximum Courant number $Co = 5$ (corresponding to a time step of 0.0002 s).

Two different subgrid scale (SGS) models were tested: the WALE model with default coefficients[62] and the dynamic KE model.[63] Simulations have included a start-up phase equal to five flow-through times $T_{\text{FT}} = W/U_{\text{FT}} = 0.61$ s (to make the flow develop and reach a condition of stable fluctuations) and then a time-averaging phase (to

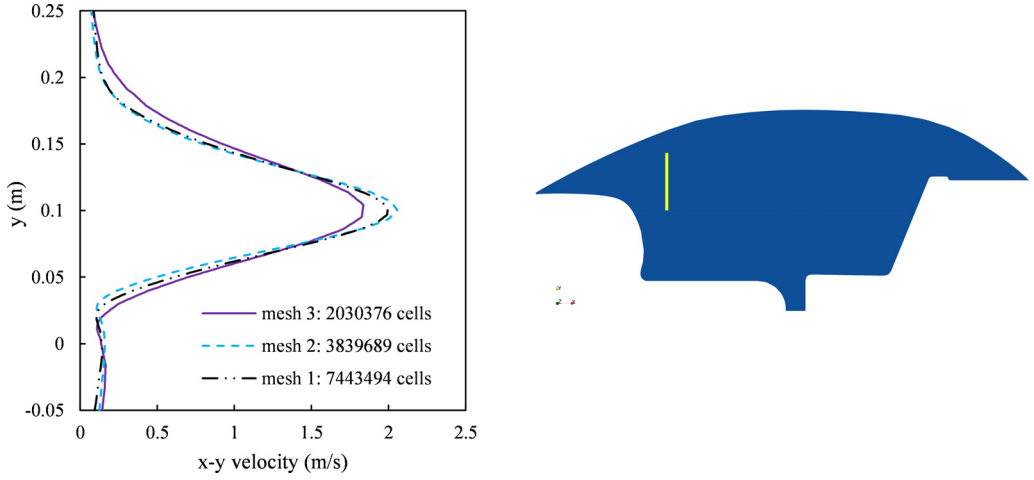

FIG. 6. Velocity profiles obtained at $x = 0.25$ m and $z = -0.03$ m (measuring plane, shown on the right), for the three grids considered in the sensitivity analysis.

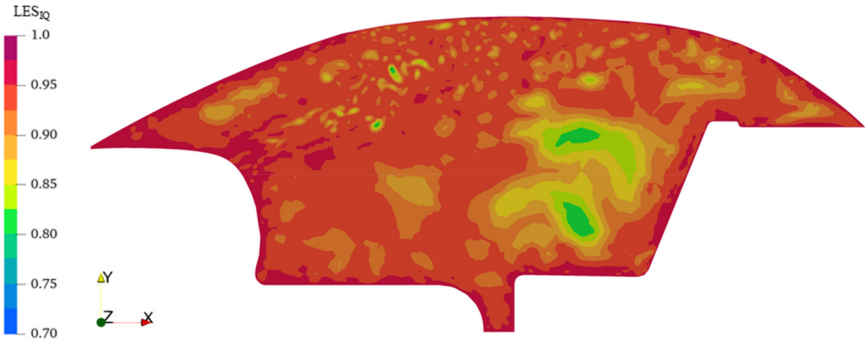

FIG. 7. Contours of LES_{IQ} on the x–y plane at $z = -0.03$ m (PIV measuring plane) for the WALE model.

get the mean solution) equal to 12 s. W (m) is the extension of the computational domain in the x direction, whereas U_{FT} (m/s) is the mean flow velocity at the inlet vents.

To assess the suitability of Mesh 1 for LES computations, the LES index of quality LES_{IQ} is calculated according to the following expression by Celik *et al.*:[64]

$$LES_{IQ} = \frac{k_{resolved}}{k_{total}} = \frac{1}{1 + 0.05 \cdot \left(\frac{\nu + \nu_{SGS}}{\nu}\right)^{0.53}}, \quad (12)$$

where ν is the molecular viscosity and ν_{SGS} is the SGS viscosity; this parameter, representing the ratio of the resolved to the total turbulent kinetic energy (TKE), must be greater than 80% for a well-resolved computation.[65] Figure 7 shows the contours of LES_{IQ} on the x–y plane at $z = -0.03$ m, for the WALE model; the minimum value is 79.4% whereas the average on the plane is 92.5%; therefore, it can be argued that the LES computations resolve a large fraction of the total turbulent kinetic energy and that the adopted grid is suitable for the investigations.

IV. NUMERICAL MODEL VALIDATION AGAINST PIV MEASUREMENTS

In this section, the validation of the numerical model is presented by comparing measured and predicted velocity fields within the longitudinal plane at $z = -0.03$ m (PIV measuring plane).

The boundary conditions imposed for the validation of the numerical model are available in Table V; I indicates the turbulence intensity, ℓ (m) is the turbulent length scale, and L (m) is the characteristic length, assumed equal to the width of the inlet sections. Patches not specified in Fig. 3 have been modeled as walls and distinguished between glazed (highlighted in light-blue color in Fig. 3) and non-glazed surfaces (highlighted in gray color in Fig. 3). Regarding temperature, non-glazed walls have been modeled as adiabatic while at glazed surfaces a fixed value has been imposed, equal to the temperature of the measurement environment during the experiments (see Sec. II A).

In URANS simulations, a Gaussian function was imposed for velocity at the inlet, defined by experimentally fitted coefficients (see Sec. II C); in LES simulations, the divergence free synthetic eddy method (DFSEM) boundary condition was adopted for the generation of synthetic turbulence, imposing the same Gaussian function for the mean velocity and mapping the Reynolds stress tensor and the turbulent length scale from the RANS solution.[66,67] Overall, the HVAC system provides an air change per hour of 60 1/h.

In Fig. 8, the experimental (bottom picture) and URANS (top picture) mean velocity contours are shown; the experimental field of view is superimposed on the CFD field to display its extent in comparison with the whole computational domain. Figure 9, instead, depicts the instantaneous velocity field predicted with the WALE model after 5 s; from this picture, it is possible to observe the jet destabilization and the turbulent mixing, aspects that cannot be captured by URANS.

In Fig. 10, mean velocity profiles in five different sections (i.e., x = 0.25, x = 0.35, x = 0.45, x = 0.55, and x = 0.65 m) are outlined; the locations where the profiles are extracted are shown in Fig. 8 with five yellow-colored vertical lines.

The capability of the URANS and LES models to reproduce the experiments was assessed quantitatively by calculating the root mean square error (RMSE) between the predicted and measured data

TABLE V. Boundary conditions set for comparison with PIV measurements.

Surface	BC for mean velocity	BC for pressure	BC for temperature	BC for k	BC for ω
Inlet sections	See Sec. II C	$\frac{\partial p}{\partial \boldsymbol{n}} = 0$	$T = 43.6\,^{\circ}\mathrm{C}$	$I = 15\%$	$\ell = 0.07$ L
Outlet section	$\frac{\partial \boldsymbol{u}}{\partial \boldsymbol{n}} = 0$	$p = 101\,325$ Pa	$\frac{\partial T}{\partial \boldsymbol{n}} = 0$	$\frac{\partial k}{\partial \boldsymbol{n}} = 0$	$\frac{\partial \omega}{\partial \boldsymbol{n}} = 0$
Glazed walls	$\boldsymbol{u} = 0$	$\frac{\partial p}{\partial \boldsymbol{n}} = 0$	$T = 30.2\,^{\circ}\mathrm{C}$	Standard wall functions	
Non-glazed walls	$\boldsymbol{u} = 0$	$\frac{\partial p}{\partial \boldsymbol{n}} = 0$	$\frac{\partial T}{\partial \boldsymbol{n}} = 0$	Standard wall functions	

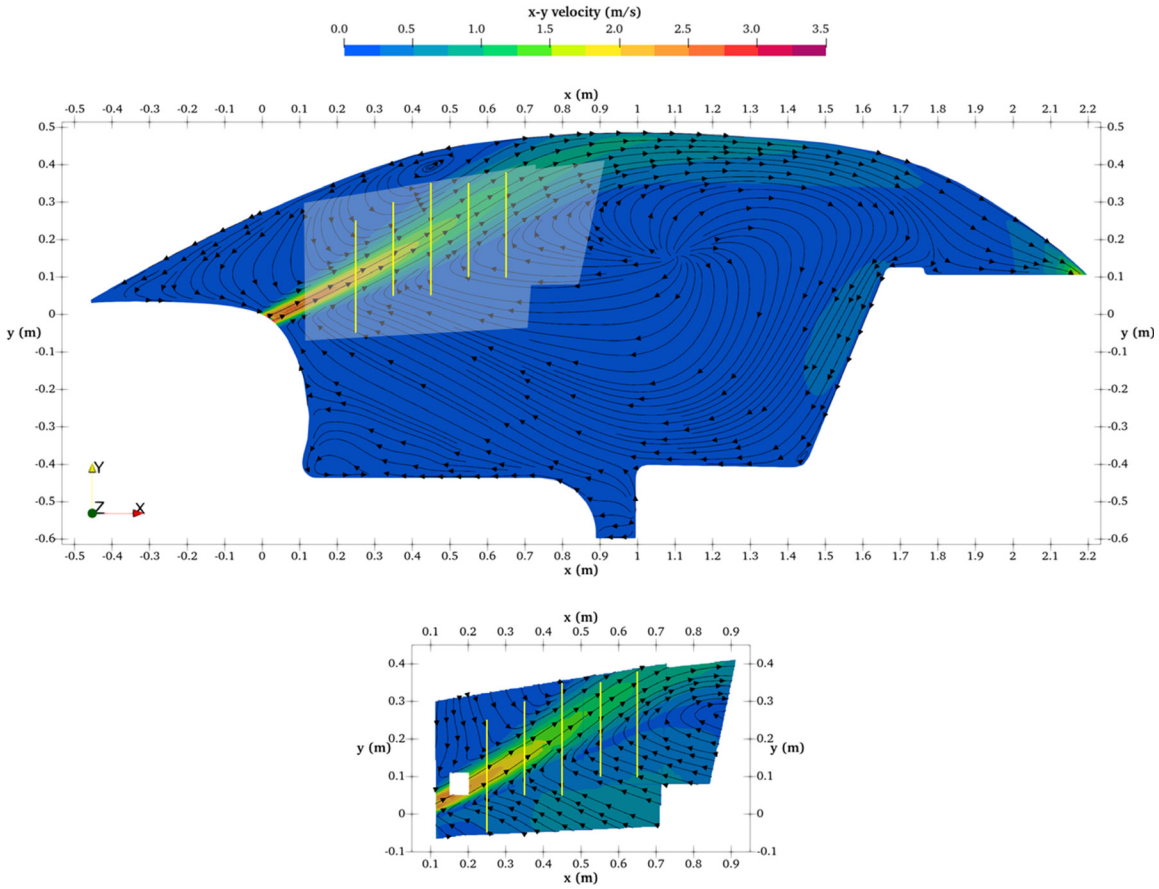

FIG. 8. URANS (top) and PIV (bottom) velocity contours on the longitudinal plane at $z = -0.03$ m (measuring plane), together with the 2D streamlines. The experimental field of view is superimposed on the CFD field.

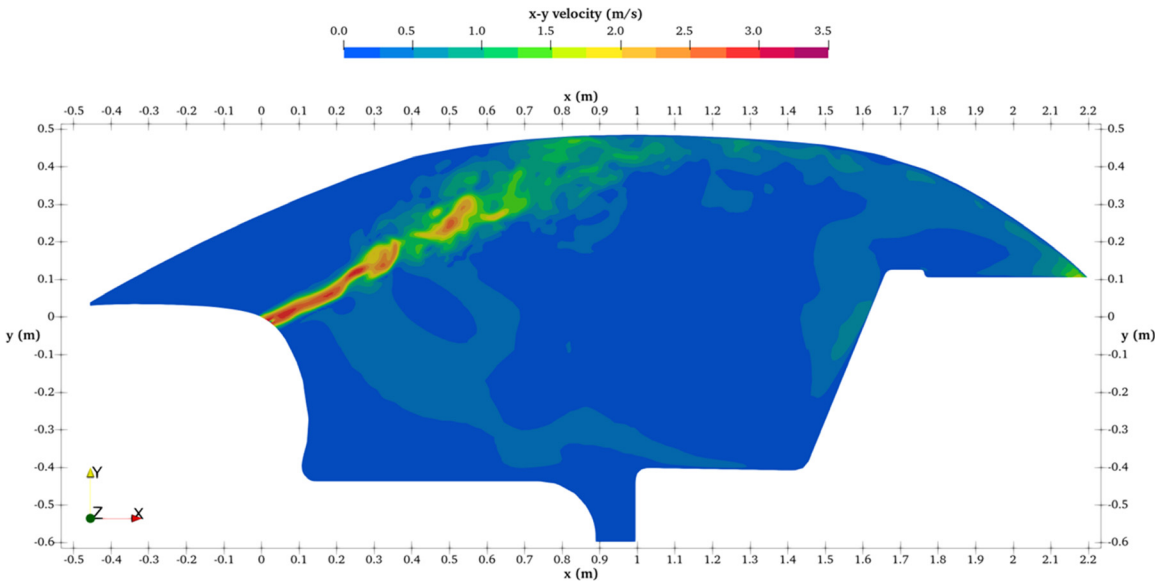

FIG. 9. Instantaneous velocity contours predicted with the WALE model, on the longitudinal plane at $z = -0.03$ m (measuring plane), after 5 s of simulated time.

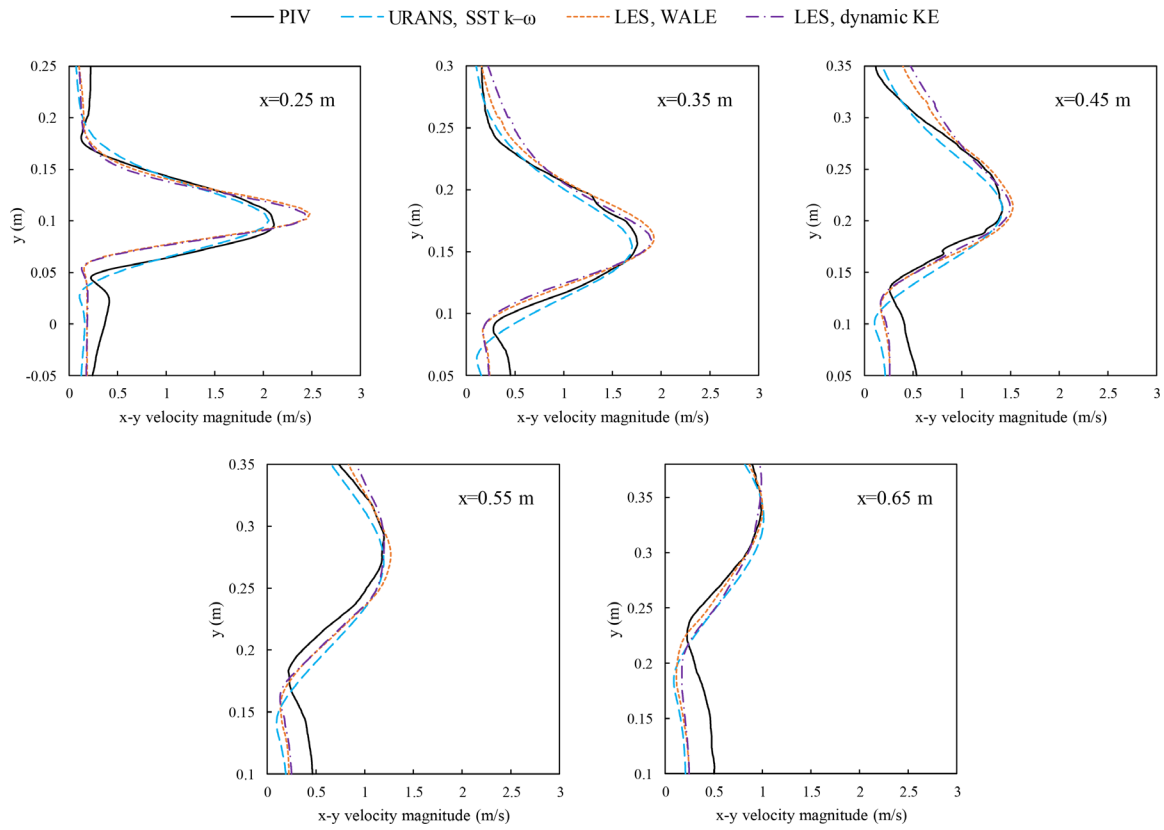

FIG. 10. Experimental and predicted velocity profiles comparison in five different sections within the selected plane at $z = -0.03$: $x = 0.25$, $x = 0.35$, $x = 0.45$, $x = 0.55$, and $x = 0.65$ m.

$$\mathrm{RMSE} = \sqrt{\frac{\sum_{i=1}^{n_p} \left(\varphi_{\mathrm{exp},i} - \varphi_{\mathrm{model},i}\right)^2}{n_p}}. \tag{13}$$

In the expression above, $\varphi_{\mathrm{exp},i}$ is a data point from the experimental data, $\varphi_{\mathrm{model},i}$ is the corresponding data point from the modeling results, and n_p is the number of points.

In addition, the normalized root mean square error (NRMSE) was calculated dividing the RMSE by the maximum velocity value measured along each profile, namely, 2.11, 1.76, 1.42, 1.20, and 0.99 m/s for $x = 0.25$, $x = 0.35$, $x = 0.45$, $x = 0.55$, and $x = 0.65$ m, respectively. The results, summarized in Table VI, show a very good agreement existing between predicted and measured velocity fields with errors below the order of 0.25 m/s (∼5% of the maximum velocity at the vent exit). In addition to the errors calculated for the five sections of interest, Table VI also provides the global errors considering the entire region where PIV measurements are available. In this case, NRMSEs are obtained dividing the RMSE by the maximum experimental velocity within the plane, which is equal to 2.49 m/s. Global values confirm the close agreement between the simulations and the experiments.

On the whole, the shape of the flow is well predicted by the CFD models; buoyancy effects are properly described as well, with profiles shifting upward when the distance from the inlet vents increases, in accordance with the experimental data.

Both LES models initially overestimate the velocity peak; this is probably because the Reynolds stress tensor given as input to the DFSEM boundary conditions is not measured but mapped from the URANS simulations. One solution to improve the accuracy of LES results could, thus, be measuring the Reynolds stress tensor at the inlet sections; this would provide a more precise description of the turbulence anisotropy and help minimize discrepancies with the PIV data. However, performing such measurements poses challenges due to the non-planar surface of the inlet vents and requires a targeted experimental campaign, which is beyond the scope of the present work. In the profiles extracted at a greater distance from the inlet, the WALE SGS model outperforms the SST k–ω, especially at $x = 0.55$ and $x = 0.65$ m. On the other hand, the dynamic KE SGS model exhibits the worst behavior and has a better agreement with PIV data only at $x = 0.55$ and $x = 0.65$ m, probably due to the initialization of the turbulent kinetic energy from precursor URANS simulation. In general, both WALE and dynamic KE models better describe the shape of the jet at the bottom; however, all models underestimate the velocity value in the area below the bulk of the jet flow. This can be primarily attributed to the simplifications made for the reproduction of the in-vehicle environment, which are more substantial in the lower part of the domain (first among all, not having modeled the presence of the steering wheel and of the gearshift, which can create disturbances to the flow field in their surroundings).

TABLE VI. RMSE and NRMSE between predicted and measured velocity values, for the five sections of interest and for the entire region where PIV measurements are available.

	RMSE (NRMSE)					
	$x = 0.25$ m	$x = 0.35$ m	$x = 0.45$ m	$x = 0.55$ m	$x = 0.65$ m	Global
URANS SST k–ω	0.142 m/s (6.7%)	0.131 m/s (7.5%)	0.176 m/s (12.4%)	0.181 m/s (15.1%)	0.189 m/s (19.1%)	0.203 m/s (8.17%)
LES WALE	0.242 m/s (11.5%)	0.130 m/s (7.4%)	0.167 m/s (11.8%)	0.143 m/s (11.9%)	0.161 m/s (16.2%)	0.207 m/s (8.34%)
LES dynamic KE	0.234 m/s (11.1%)	0.158 m/s (9.0%)	0.182 m/s (12.8%)	0.133 m/s (11.1%)	0.155 m/s (15.6%)	0.206 m/s (8.29%)

Overall, the URANS SST k–ω model is sufficiently accurate in predicting the airflow patterns (if proper attention is given to the design of the CFD simulation) and is appreciably outperformed by LES only in the turbulent mixing region.

A more careful comparisons between the simulated and measured mean flow fields can be made considering the distributions of the mean z-vorticity (Ω_z, 1/s) shown in Fig. 11, where the positive z-direction is oriented away from the x–y plane. The numerical fields are represented on the PIV measuring plane for a more effective visualization.

The mean z-vorticity contours in Fig. 11 emphasize the capability of all the adopted models in predicting the mean flow structures, both inside and outside the main bulk of the jet. In fact, the strong vortices at the edges of the jet (arising from the interaction of the moving jet with the still surroundings) are well reproduced as well as the vorticity distribution away from the jet core.

The close agreement between the experimental and numerical data is confirmed when looking at Fig. 12, which displays the difference between the predicted and measured z-vorticity. Outside of the jet core, the absolute difference is almost everywhere below 10 1/s; the largest differences are located in the bottom-left corner, confirming that the simplification of the geometry in the lower part of the domain can reduce the accuracy of the numerical models in reproducing the flow characteristics in that area.

To assess the performance of the adopted CFD models in predicting not only the mean flow behavior but also the fluctuations in the velocity fields, a comparison between numerical and PIV data is made in terms of turbulent kinetic energy (TKE). Figure 13 displays the measured and predicted TKE fields (with the latter represented on the PIV measuring plane for effective visualization), while Fig. 14 presents a comparison across the same five sections previously analyzed (i.e., $x = 0.25$, $x = 0.35$, $x = 0.45$, $x = 0.55$, and $x = 0.65$ m). Overall, the LES simulations yield higher TKE values than URANS simulations, resulting in better agreement with the measured values except at $x = 0.25$ m. In this section, the LES models exhibit higher RMSEs than URANS, attributed to upward shifts in the profiles (as observed in Fig. 10 for the velocity profiles). Nevertheless, the LES models provide a better prediction of the profile shape. Table VII summarizes the RMSE and

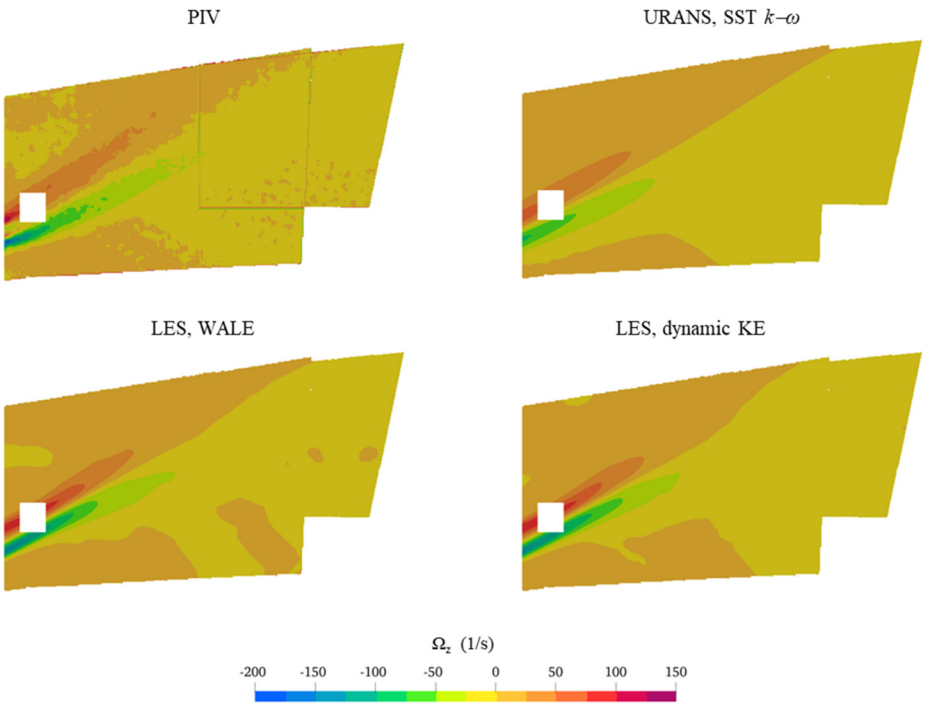

FIG. 11. Experimental and numerical distribution of the mean z–vorticity. The numerical fields are represented on the PIV measuring plane for a more effective visualization.

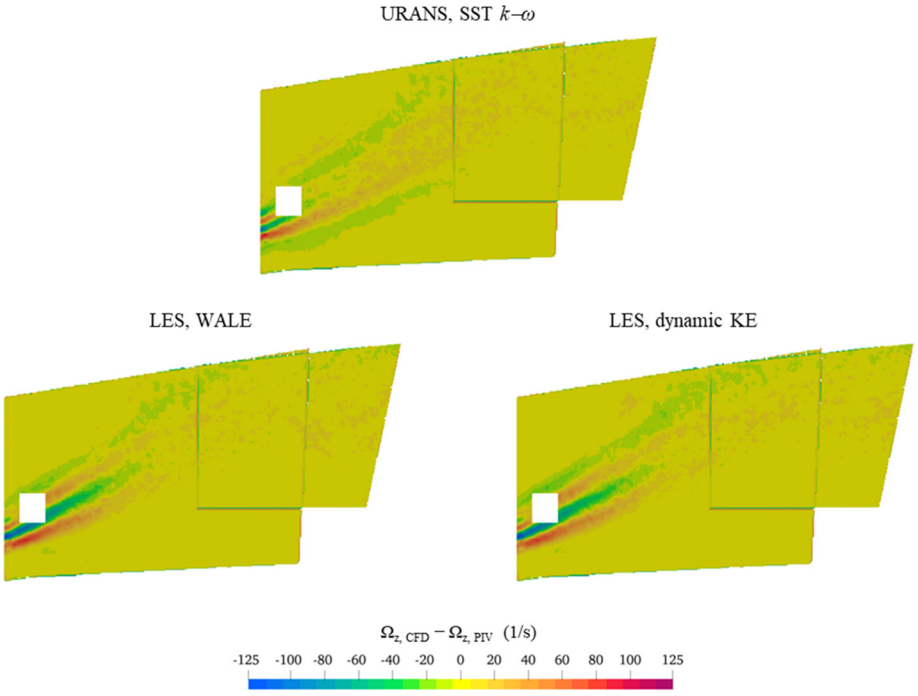

FIG. 12. Spatial distribution of the difference between the predicted and measured z-vorticity, obtained with the different turbulence models.

NRMSE values obtained for the different sections of interest and for the entire region where PIV measurements are available. NRMSE values are calculated by dividing the RMSE by the maximum experimental value along each profile (namely, 0.563, 0.603, 0.509, 0.444, and 0.337 m^2/s^2 for $x = 0.25$, $x = 0.35$, $x = 0.45$, $x = 0.55$, and $x = 0.65$ m, respectively) for errors calculated for each profile, and the maximum within the whole measuring plane for global values (i.e., 0.637 m^2/s^2).

Although the dynamic KE model shows worse agreement with experiments than the WALE model in the five investigated sections, it has lower global errors. This can be explained by examining Fig. 15,

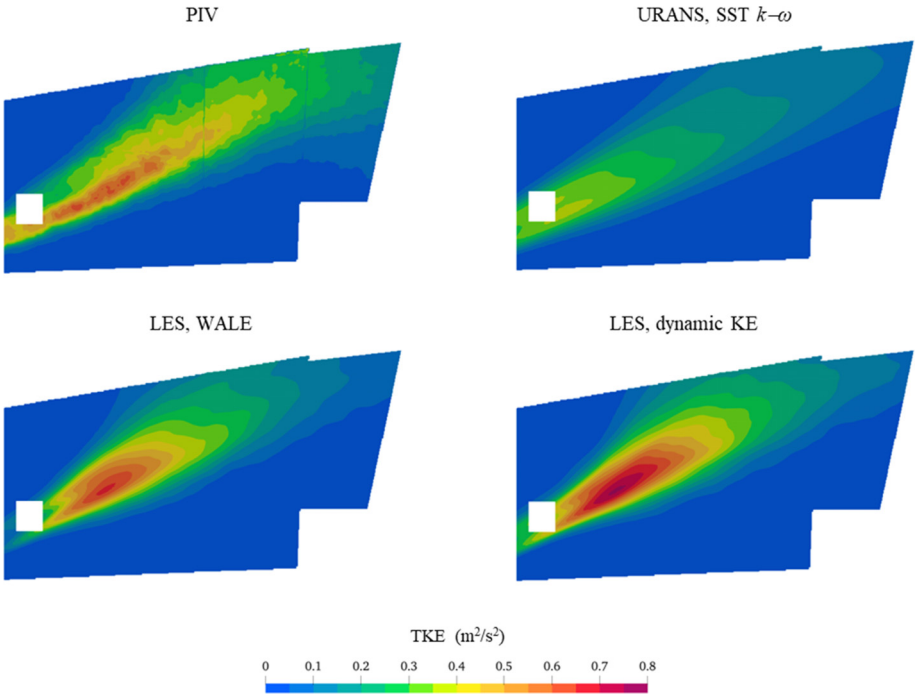

FIG. 13. Experimental and numerical distribution of the turbulent kinetic energy. The numerical fields are represented on the PIV measuring plane for a more effective visualization.

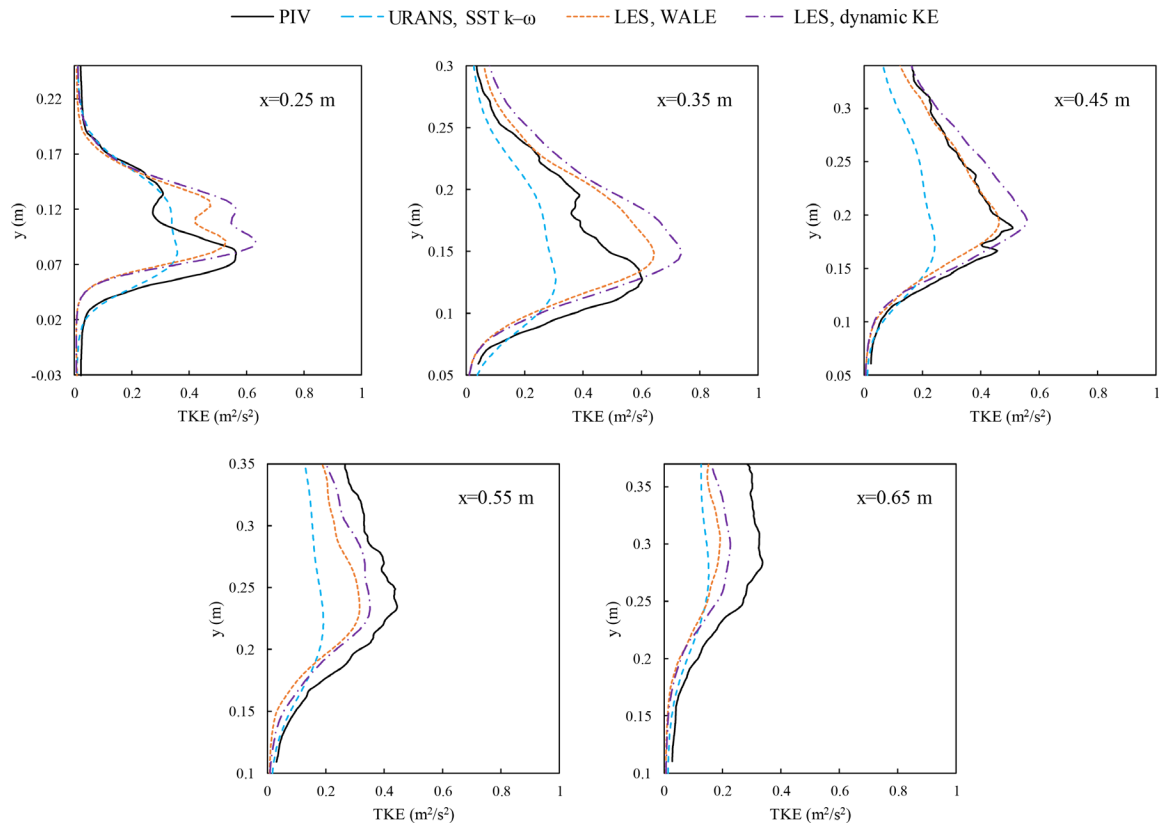

FIG. 14. Experimental and predicted turbulent kinetic energy profiles comparison in five different sections within the selected plane at $z = -0.03$ m: $x = 0.25$, $x = 0.35$, $x = 0.45$, $x = 0.55$, and $x = 0.65$ m.

which displays the difference between predicted and measured TKE for all turbulence models. In the jet core, the dynamic KE exhibits worse agreement, while the WALE model demonstrates a poorer performance in the bottom-left region (closer to the inlet sections), resulting in a slightly worse overall agreement with the experiments. Figure 15 also highlights that the URANS SST k–ω underestimates the TKE in the jet core, and all models underestimate the TKE in the bottom-left region.

The simulations were performed on a Dell Precision 7920 Rack with 104 CPUs and 64 GB RAM. URANS computations took 4.7 days to complete on the finest grid; LES took about twice the time required by URANS. Due to the less computational resources required, URANS approach has been selected for the numerical investigations presented in Sec. V.

V. DISCUSSION OF VELOCITY AND TEMPERATURE FIELDS, AND THERMAL COMFORT ANALYSIS

The validated URANS model is here applied to study the thermal-fluid dynamics fields inside the car cabin in winter and summer conditions. The same boundary conditions as the validation scenario were adopted, with the exception of the temperature values at the inlet sections and at the glazed walls, listed in Table VIII and

TABLE VII. RMSE and NRMSE between predicted and measured TKE values, for the five sections of interest and for the entire region where PIV measurements are available.

	RMSE (NRMSE)					
	$x = 0.25$ m	$x = 0.35$ m	$x = 0.45$ m	$x = 0.55$ m	$x = 0.65$ m	Global
URANS SST k–ω	0.067 m²/s² (11.98%)	0.140 m²/s² (23.16%)	0.133 m²/s² (26.18%)	0.158 m²/s² (35.61%)	0.118 m²/s² (34.96%)	0.101 m²/s² (15.90%)
LES WALE	0.097 m²/s² (17.30%)	0.098 m²/s² (16.26%)	0.035 m²/s² (6.81%)	0.092 m²/s² (20.64%)	0.101 m²/s² (29.85%)	0.085 m²/s² (13.27%)
LES dynamic KE	0.120 m²/s² (21.24%)	0.133 m²/s² (22.07%)	0.053 m²/s² (10.38%)	0.062 m²/s² (13.85%)	0.078 m²/s² (23.16%)	0.080 m²/s² (12.55%)

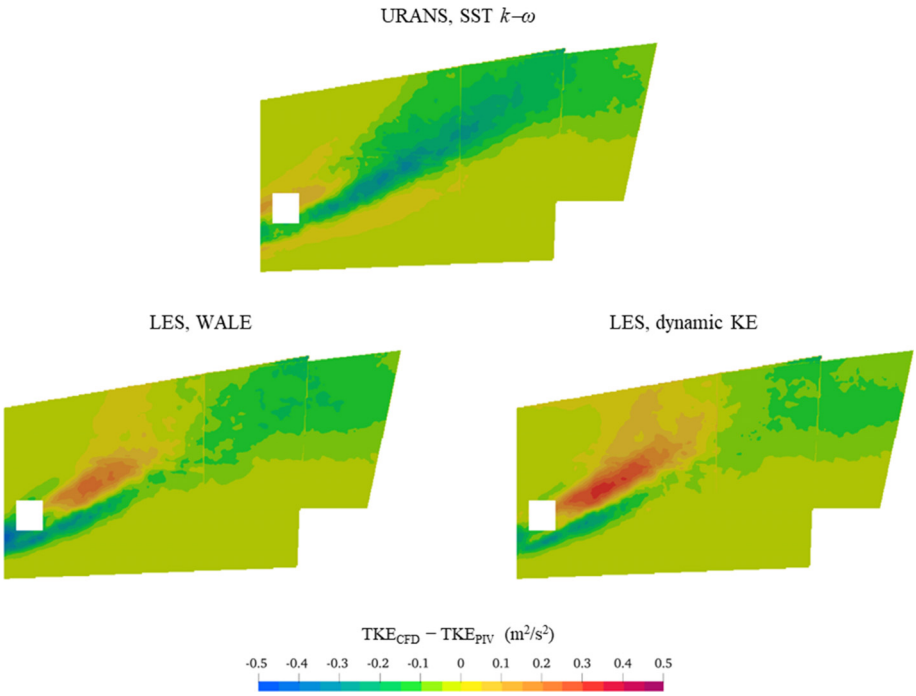

FIG. 15. Spatial distribution of the difference between the predicted and measured turbulent kinetic energy, obtained with the different turbulence models.

TABLE VIII. Subset of boundary conditions imposed for temperature in winter and summer scenarios.

Surface	Winter scenario	Summer scenario
Inlet sections	$T = 20\,^{\circ}\mathrm{C}$	$T = 25\,^{\circ}\mathrm{C}$
Glazed walls	$T = 10\,^{\circ}\mathrm{C}$	$T = 30\,^{\circ}\mathrm{C}$

selected according to the climatic conditions outlined in Sec. II D. Since the thermal resistance of windows and windshield is negligible (due to their fine thickness and to the large convection heat transfer coefficients in forced convection), it is reasonable to assume the glazed walls temperature equal to the outdoor temperature.

Investigated scenarios cover 10 min of simulated time, which are sufficient to achieve a quasi-steady state condition (as discussed in Sec. V A). Five virtual probes were placed in the computational domain as shown in Fig. 16, representing the position of the passengers, to monitor the evolution over time of PMV and PPD indices; such an approach allows us to find out whether the thermal comfort of the passengers is ensured and to determine the amount of time required to achieve acceptable thermo-hygrometric conditions.

Mean temperature and velocity fields are also discussed by comparing winter and summer scenarios.

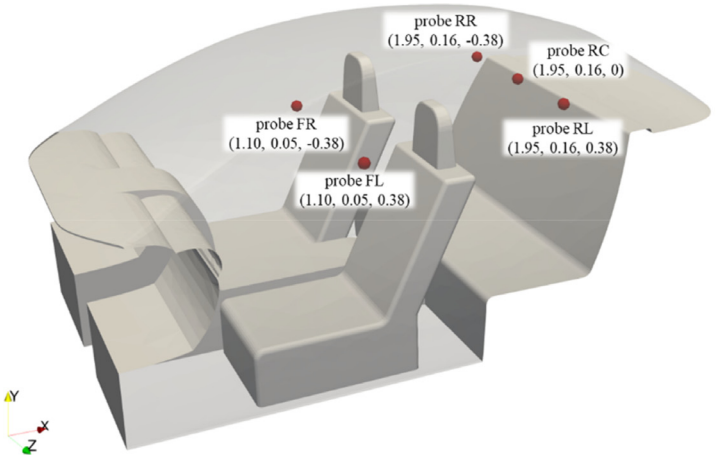

Abbreviations

FL: Front Left
FR: Front Right
RL: Rear Left
RC: Rear Center
RR: Rear Right

FIG. 16. Positions inside the domain, with coordinates expressed in meters, of the virtual probes placed to monitor the evolution over time of PMV and PPD.

A. Numerical mean velocity and temperature fields

In the present section, mean velocity and temperature fields are discussed by comparing winter and summer scenarios.

In Fig. 17, the trend over time of temperature and velocity values in correspondence of the five virtual probes is depicted. After 60 s, the velocity field already has stable fluctuations whereas, as expected, thermal phenomena have a longer evolution time and 300 s are required to reach a steady state. The averaging time interval was selected accordingly, discarding the first minutes and considering from the fifth minute (i.e., 300 s) onward; in so doing, the mean temperature fields are not affected by the initial transients and the mean velocity fields are not affected by the initial thermal instabilities.

Figure 18 shows the streamlines of the airflow entering the domain from the inlet vents, colored by mean velocity, in winter and summer scenarios. Motion structures are very similar, with the jet flows directed toward the rear compartment without being deflected and creating a recirculating zone near the rear seats; the different thermal regime has a very little effect on the velocity fields, since the temperature field is fairly uniform as can be seen by Figs. 19 and 20, where temperature contours are displayed on the x–y slices intersecting the driver and passenger seats, respectively. Only a small difference can be observed in the direction of the central jets that in winter scenario are slightly shifted upward owing to the buoyancy forces.

The small influence of temperature field on the airflow patterns is confirmed by comparing velocity contours and streamlines in winter and summer on the driver [Fig. 21(a) vs Fig. 21(b)] and passenger side [Fig. 22(a) vs Fig. 22(b)]. Flow patterns are very similar, with the air directed toward the parcel shelf and a recirculating zone being created in the rear compartment.

A further aspect which must be addressed is the influence of the asymmetric air supply by the HVAC system on the velocity fields. By comparing Fig. 21(a) with Fig. 22(a) (winter conditions) and Fig. 21(b) with Fig. 22(b) (summer conditions), it is possible to observe that the passenger side is characterized by higher velocities, and this is due by the higher velocity of the air supplied by the right vents with respect to the left vents (see Table II and Fig. 4). However, this asymmetry does not affect the thermal comfort of the occupants dramatically, as discussed in Sec. V B, since such differences are confined to the upper part of the passenger compartment.

Finally, in Fig. 23, the mean z velocity contours are shown, together with the 2D streamlines, for the x–z plane intersecting the mouth of possible passengers (i.e., at $y = 0.1$ m), for winter and summer scenarios. In this case, important differences can be highlighted both in flow patterns and velocity values. On the other hand, in both conditions, the velocity component in the z direction is not negligible and there are significant recirculation zones in the rear seats; in addition, in the front seats, the streamlines are directed from the two sides

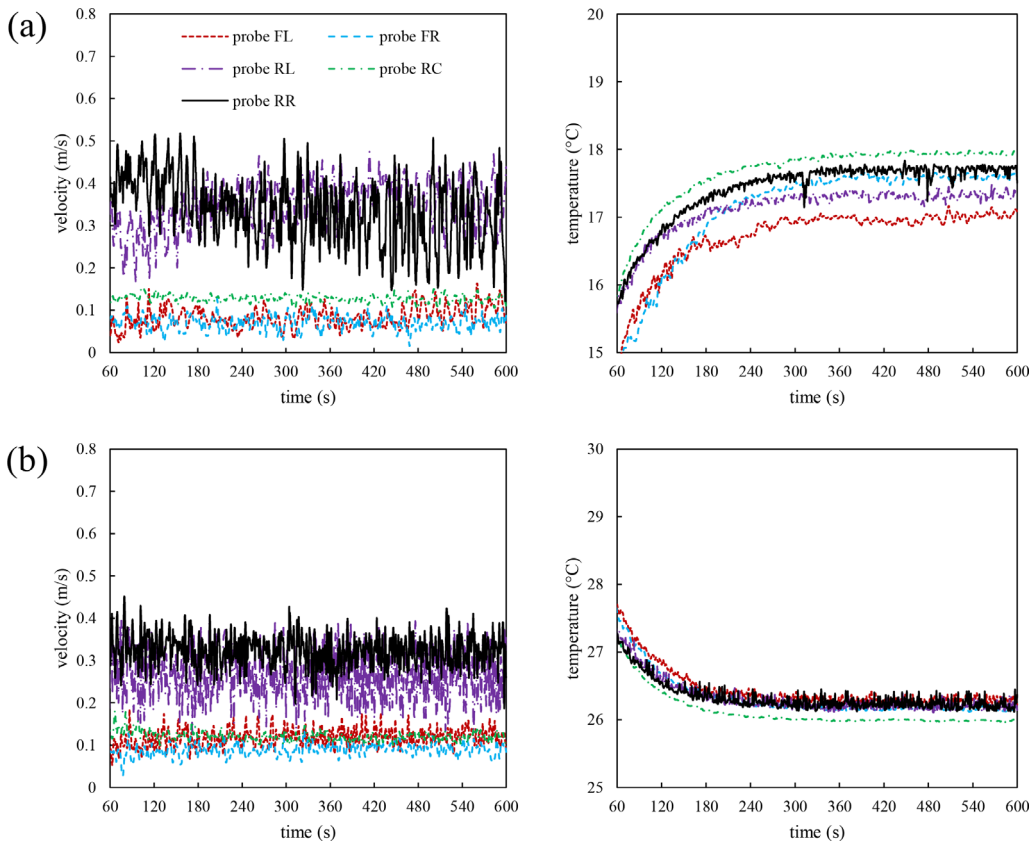

FIG. 17. Trend over time of velocity and temperature values in correspondence of the five virtual probes placed in the domain for (a) winter and (b) summer conditions.

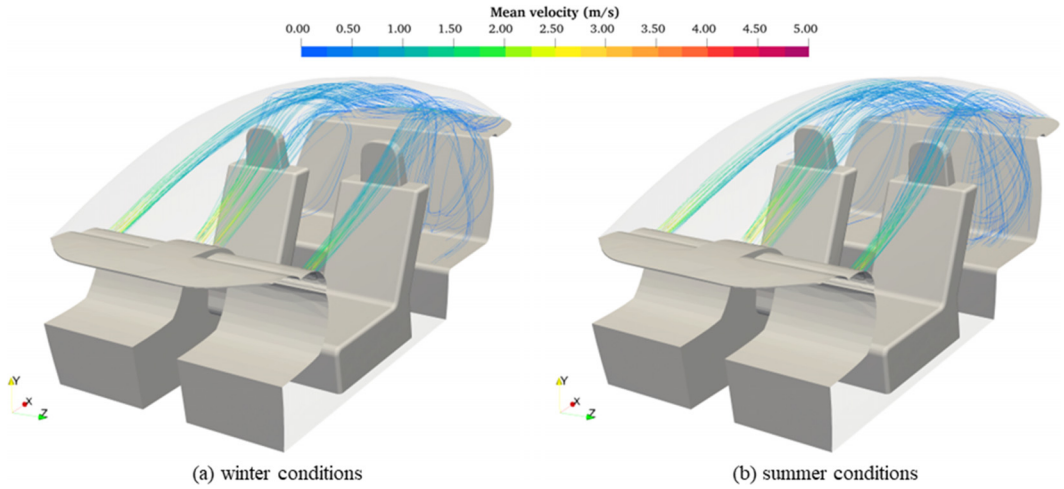

FIG. 18. Streamlines of the airflows entering the domain from the inlet vents, colored by mean velocity magnitude, for (a) winter and (b) summer conditions.

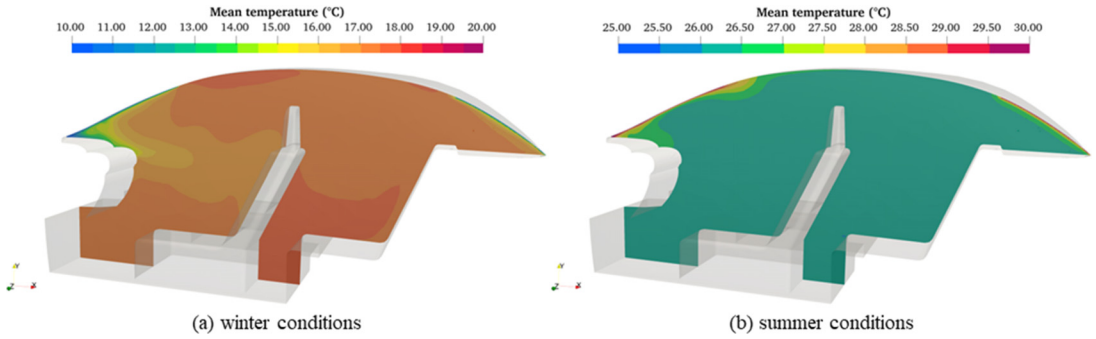

FIG. 19. Mean temperature contours on the driver side (x–y slice at $z = 0.38$ m, i.e., driver's seat) for (a) winter and (b) summer conditions.

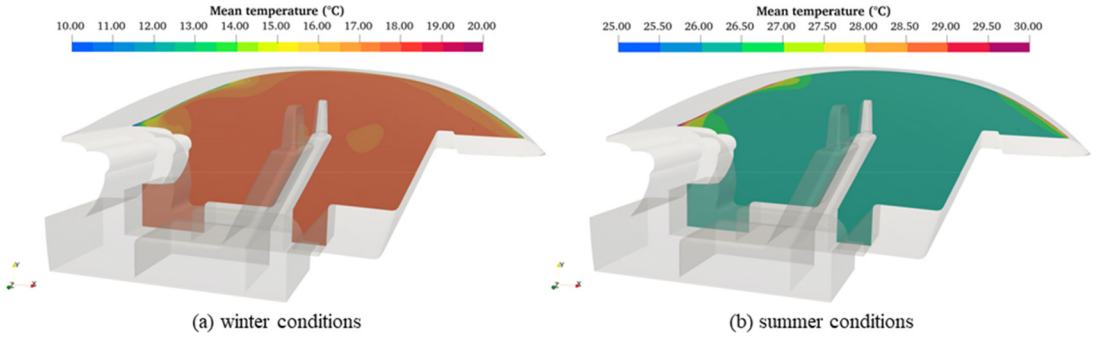

FIG. 20. Mean temperature contours on the passenger side (x–y slice at $z = -0.38$ m, i.e., passenger's seat) for (a) winter and (b) summer conditions.

toward the center. All these three features may be decisive in the transmission of respiratory viruses, thus posing a risk for the occupants.

It must be pointed out that the presence of the passengers would definitely affect the air flow patterns inside the car cabin and their contribution inside a real cabin environment will be studied in future works. The main scope of the present work is, in fact, to numerically reproduce the experiments (so developing a reliable validated tool to be used for many purposes) and to give insight in the design of CFD simulations of a real car cabin. Since the PIV measurements were taken in the absence of occupants, the latter was not included in the numerical simulations. In addition, such an approach allows us to isolate the only contribution of the HVAC system, which has been proven

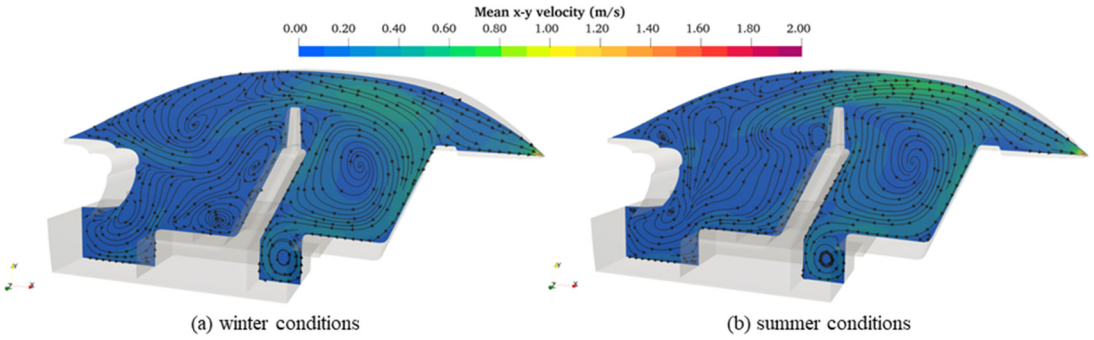

FIG. 21. Mean x–y velocity contours and 2D streamlines on the driver side (x–y slice at $z = 0.38$ m) for (a) winter and (b) summer conditions.

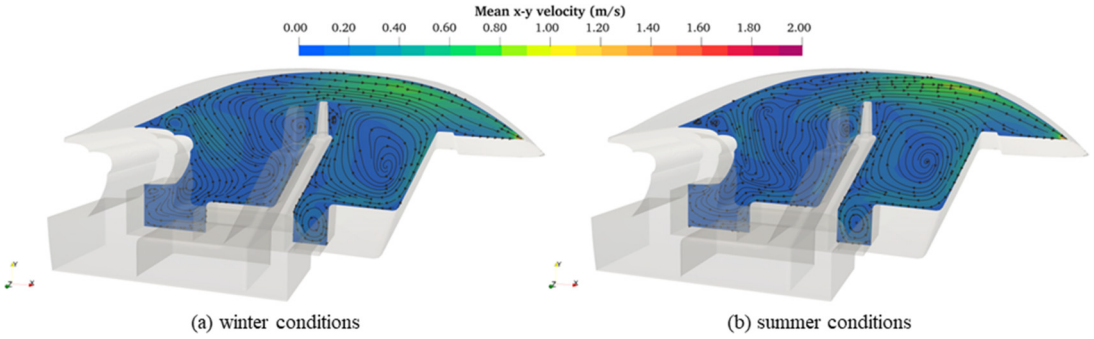

FIG. 22. Mean x–y velocity contours and 2D streamlines on the passenger side (x–y slice at $z = -0.38$ m) for (a) winter and (b) summer conditions.

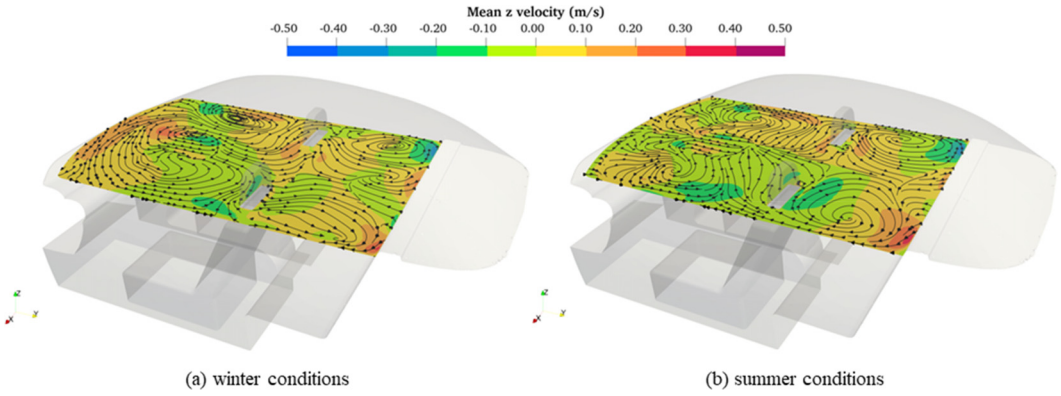

FIG. 23. Mean z velocity contours and 2D streamlines on the x–z slice at $y = 0.1$ m for (a) winter and (b) summer conditions.

to have a strong influence on the distribution of exhaled respiratory droplets inside car cabins.[29,30]

B. Thermal comfort assessment

As explained in Sec. II E, PMV and PPD indices were evaluated according to the ISO 7730 Standard using the *pythermalcomfort* package.[58] The mean radiant temperature was calculated as the average walls temperature; the relative humidity was determined according to the model developed in Ref. 68, based on the moisture balance; the metabolic rate was set to 1.5 met (1 metabolic unit = 1 met = 58.2 W/m^2) for the driver and to 1.2 met for other passengers,[58] and the clothing insulation set to 0.5 clo (1 clothing unit = 1 clo = 0.155 m^2 K/W) for typical summer garment and to 1 clo for typical winter garment.[58]

Results are presented in graphical form in Figs. 24 and 25, where the comfort region (PMV in the range −0.5 to 0.5, resulting in a PPD under 10%) is highlighted in green color.

In winter conditions [Figs. 24(a) and 25(a)], the negative values of the PMV mean that the occupants are cold; after initial unacceptable values, the operation of the HVAC system allows us to improve the

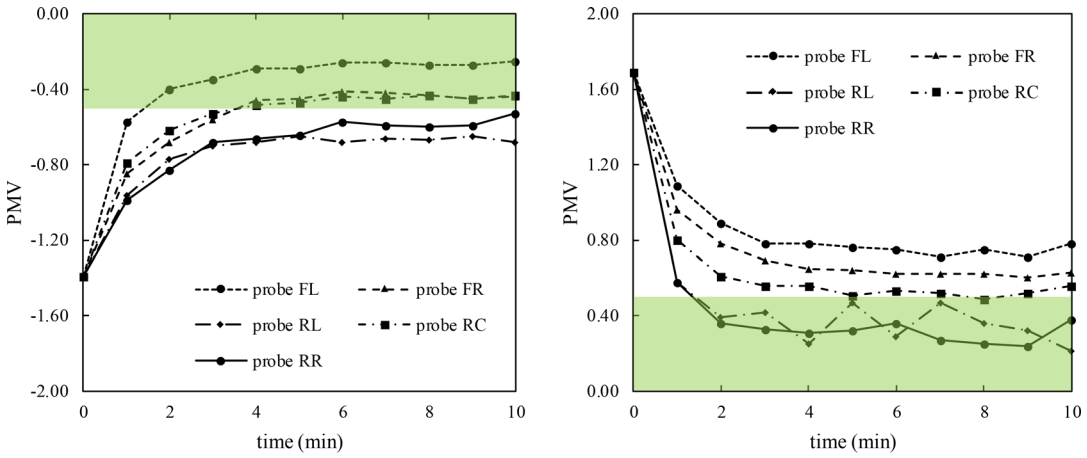

FIG. 24. PMV in correspondence of the virtual probes, for (a) winter and (b) summer conditions.

thermal sensation of the people in the cabin and after 5 min a quasi-steady state regime is achieved. Due to the higher metabolic activity, the driver (probe FL) experiences the best condition, with a PMV well above the lower limit of −0.5 (PPD well below 10%); a good condition is also experienced by the passengers sitting next to the driver (probe FR) and on the central back seat (probe RC). For what concerns the passengers sitting on the left back seat (probe RL) and right back seat (probe RR), the comfort indices exceed the bounds owing to the higher air speeds (see Figs. 21 and 22); however, the comfort indices fall in the lowest class (i.e., class C) and the environment can still be considered acceptable. In summer [Figs. 24(b) and 25(b)], the occupants share a hot environment as evidenced by the positive values of the PMV. In such scenario, the higher metabolic activity disadvantages the driver, who experiences the worst condition (PMV > 0.7, PPD > 15%) followed by the passengers sitting next to the driver (probe FR) and on the central back seat (probe RC). In this case, the higher velocities improve the comfort sensation of passengers sitting on the left back seat (probe RL) and right back seat (probe RR), which have PMV < 0.5 (PPD < 10%). Despite the asymmetry of the fan strengths and the different air velocities, the PMV in correspondence of probes RL and RR is close to each other both in winter and summer.

A general consideration, referred to both scenarios, is that thermal comfort sensation can be quite different for passengers sitting on different seats, as a function of different temperature and velocity values as well as of the different metabolic activity; this aspect should be duly taken into account when designing and operating the heating ventilation and air conditioning system, since the minimum comfort requirements should be met for all occupants sharing the car. In this respect, validated CFD tools can be very useful since they allow us to predict and to design the airflow patterns inside the car cabin.

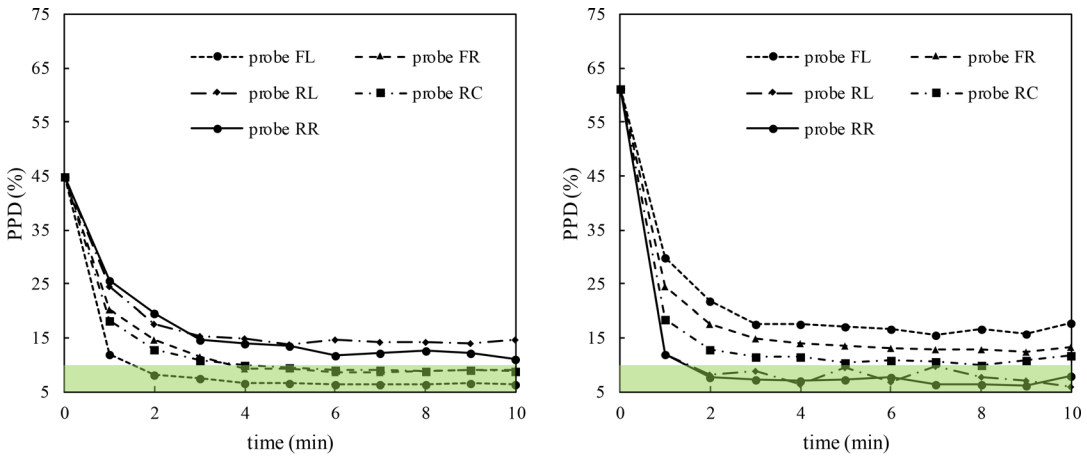

FIG. 25. PPD in correspondence of the virtual probes, for (a) winter and (b) summer conditions.

VI. CONCLUSIONS

In the present paper, we developed a transient non-isothermal CFD tool, validated against PIV measurements, able to predict the airflow patterns inside a real car cabin. The main objective is to give insight in the design of CFD simulations of such indoor microenvironments and to produce a reliable tool to be used for many purposes, including the improvement of IAQ and comfort of the occupants and the reduction in the energy consumption by the HVAC system. Numerical analyses have been carefully designed, giving attention to the reproduction of the in-vehicle environment, identification of inlet and outlet sections, and the proper definition of the boundary conditions; all this led to a very good numerical–experimental agreement, with errors kept below 0.25 m/s for the mean velocity.

A comparison is made between URANS (with the SST k–ω model) and LES (with the WALE and dynamic KE models) approaches, evidencing that the URANS produces satisfactory results and is suitable for studying the thermal-fluid dynamics fields inside real car cabins.

The URANS model, owing to the less computational resources required, is applied to characterize the mean thermal-fluid dynamics fields in winter and summer conditions and to assess the evolution over time of the PMV and the PPD indices at multiple points of the cabin representing the position of the passengers. In quasi-steady state conditions, the temperature is fairly uniform inside the cabin, and therefore, has a little influence on the velocity fields; the direct consequence is that the mean flow structures in summer and winter are very similar.

On the other hand, the analysis of the well-being of the occupants here performed led to the conclusion that passengers sharing the same car may have contrasting comfort perceptions. This point must be considered in the design and operation of the HVAC systems, since the environment must meet the minimum comfort requirements for all the occupants; to this end, validated CFD tools become essential as they allow us to faithfully predict the airflow patterns in this and other indoor environments.

In this study, the presence of the passengers in the car cabin was not modeled, since the experiments were conducted in the absence of occupants; this aspect will be addressed in future studies, relying on the CFD tool here validated.

AUTHOR DECLARATIONS

Conflict of Interest

The authors have no conflicts to disclose.

Author Contributions

Giorgio Grossi: Data curation (equal); Investigation (equal); Methodology (equal); Software (equal); Validation (equal); Writing – original draft (equal); Writing – review & editing (equal). **Fausto Arpino:** Conceptualization (equal); Formal analysis (equal); Methodology (equal); Supervision (equal); Writing – review & editing (equal). **Michele Bertone:** Data curation (equal); Investigation (equal); Validation (equal). **Gino Cortellessa:** Conceptualization (equal); Formal analysis (equal); Methodology (equal); Supervision (equal); Writing – review & editing (equal). **Andrea Sciacchitano:** Conceptualization (equal); Formal analysis (equal); Methodology (equal); Supervision (equal); Writing – review & editing (equal).

DATA AVAILABILITY

The data that support the findings of this study are available from the corresponding author upon reasonable request.

REFERENCES

[1]R. You, C. Lin, D. Wei, and Q. Chen, "Evaluating the commercial airliner cabin environment with different air distribution systems," Indoor Air **29**(5), 840–853 (2019).
[2]R. You, J. Chen, Z. Shi, W. Liu, C.-H. Lin, D. Wei, and Q. Chen, "Experimental and numerical study of airflow distribution in an aircraft cabin mock-up with a gasper on," J. Build. Perform. Simul. **9**(5), 555–566 (2016).
[3]W. Liu, J. Wen, C.-H. Lin, J. Liu, Z. Long, and Q. Chen, "Evaluation of various categories of turbulence models for predicting air distribution in an airliner cabin," Build. Environ. **65**, 118–131 (2013).
[4]C. Yang, X. Zhang, Z. Yao, X. Cao, J. Liu, and F. He, "Numerical study of the instantaneous flow fields by large eddy simulation and stability analysis in a single aisle cabin model," Build. Environ. **96**, 1–11 (2016).
[5]W. Liu, S. Mazumdar, Z. Zhang, S. B. Poussou, J. Liu, C.-H. Lin, and Q. Chen, "State-of-the-art methods for studying air distributions in commercial airliner cabins," Build. Environ. **47**, 5–12 (2012).
[6]C. Wu and N. A. Ahmed, "A novel mode of air supply for aircraft cabin ventilation," Build. Environ. **56**, 47–56 (2012).
[7]J. Fišer and M. Jícha, "Impact of air distribution system on quality of ventilation in small aircraft cabin," Build. Environ. **69**, 171–182 (2013).
[8]Y. Yan, X. Li, Y. Shang, and J. Tu, "Evaluation of airborne disease infection risks in an airliner cabin using the Lagrangian-based Wells-Riley approach," Build. Environ. **121**, 79–92 (2017).
[9]R. You, J. Chen, C.-H. Lin, D. Wei, and Q. Chen, "Investigating the impact of gaspers on cabin air quality in commercial airliners with a hybrid turbulence model," Build. Environ. **111**, 110–122 (2017).
[10]R. You, Y. Zhang, X. Zhao, C.-H. Lin, D. Wei, J. Liu, and Q. Chen, "An innovative personalized displacement ventilation system for airliner cabins," Build. Environ. **137**, 41–50 (2018).
[11]J.-H. Thysen, T. Van Hooff, B. Blocken, and G. J. F. Van Heijst, "CFD simulations of two opposing plane wall jets in a generic empty airplane cabin: Comparison of RANS and LES," Build. Environ. **205**, 108174 (2021).
[12]Q. Cao, M. Liu, X. Li, C.-H. Lin, D. Wei, S. Ji, T. Zhang, and Q. Chen, "Influencing factors in the simulation of airflow and particle transportation in aircraft cabins by CFD," Build. Environ. **207**, 108413 (2022).
[13]V. Bianco, O. Manca, S. Nardini, and M. Roma, "Numerical investigation of transient thermal and fluid dynamic fields in an executive aircraft cabin," Appl. Therm. Eng. **29**(16), 3418–3425 (2009).
[14]P. Zítek, T. Vyhlídal, G. Simeunović, L. Nováková, and J. Čížek, "Novel personalized and humidified air supply for airliner passengers," Build. Environ. **45**(11), 2345–2353 (2010).
[15]R. R. Rajendran, F. E. Ţurcanu, R. Md. Tawfiqur, and H. Askarpour, "Computational fluid dynamic analysis of corona virus patients breathing in an airplane," Phys. Fluids **35**(3), 035129 (2023).
[16]K. Talaat, M. Abuhegazy, O. A. Mahfoze, O. Anderoglu, and S. V. Poroseva, "Simulation of aerosol transmission on a Boeing 737 airplane with intervention measures for COVID-19 mitigation," Phys. Fluids **33**(3), 033312 (2021).
[17]M. Liu, J. Li, J. Liu, and M. A. Hassan, "Turbulence characterization of instantaneous airflow above passengers with different air distribution systems in a commercial airliner cabin," Phys. Fluids **35**(8), 085118 (2023).
[18]N. Li, L. Yang, X. Li, X. Li, J. Tu, and S. C. P. Cheung, "Multi-objective optimization for designing of high-speed train cabin ventilation system using particle swarm optimization and multi-fidelity Kriging," Build. Environ. **155**, 161–174 (2019).
[19]M. Visone, M. Lanzetta, M. Lappa, C. Lanzaro, and L. Polizio, "Three-dimensional simulation of clouds of multi-disperse evaporating saliva droplets in a train cabin," Phys. Fluids **33**(8), 083318 (2021).
[20]C. Peña-Monferrer, S. Antao, and R. Manson-Sawko, "Numerical investigation of droplets in a cross-ventilated space with sitting passengers under asymptomatic virus transmission conditions," Phys. Fluids **33**(12), 123314 (2021).

[21]F. Li, E. S. Lee, B. Zhou, J. Liu, and Y. Zhu, "Effects of the window openings on the micro-environmental condition in a school bus," Atmos. Environ. **167**, 434–443 (2017).
[22]S. Zhu, J. Srebric, J. D. Spengler, and P. Demokritou, "An advanced numerical model for the assessment of airborne transmission of influenza in bus microenvironments," Build. Environ. **47**, 67–75 (2012).
[23]S. Zhu, P. Demokritou, and J. Spengler, "Experimental and numerical investigation of micro-environmental conditions in public transportation buses," Build. Environ. **45**(10), 2077–2088 (2010).
[24]Q. Luo, C. Ou, J. Hang, Z. Luo, H. Yang, X. Yang, X. Zhang, Y. Li, and X. Fan, "Role of pathogen-laden expiratory droplet dispersion and natural ventilation explaining a COVID-19 outbreak in a coach bus," Build. Environ. **220**, 109160 (2022).
[25]Z. Zhang, T. Han, K. H. Yoo, J. Capecelatro, A. L. Boehman, and K. Maki, "Disease transmission through expiratory aerosols on an urban bus," Phys. Fluids **33**(1), 015116 (2021).
[26]Y. Yang, Y. Wang, L. Tian, C. Su, Z. Chen, and Y. Huang, "Effects of purifiers on the airborne transmission of droplets inside a bus," Phys. Fluids **34**(1), 017108 (2022).
[27]Y. Yang, Y. Wang, C. Su, X. Yuan, X. Liu, and Z. Chen, "A rapid method for prediction of airborne disease infection risks in an intercity bus," Phys. Fluids **34**(8), 083323 (2022).
[28]C. C. Ooi, A. Suwardi, Z. L. Ou Yang, G. Xu, C. K. I. Tan, D. Daniel, H. Li, Z. Ge, F. Y. Leong, K. Marimuthu, O. T. Ng, S. B. Lim, P. Lim, W. S. Mak, W. C. D. Cheong, X. J. Loh, C. W. Kang, and K. H. Lim, "Risk assessment of airborne COVID-19 exposure in social settings," Phys. Fluids **33**(8), 087118 (2021).
[29]F. Arpino, G. Cortellessa, G. Grossi, and H. Nagano, "A Eulerian-Lagrangian approach for the non-isothermal and transient CFD analysis of the aerosol airborne dispersion in a car cabin," Build. Environ. **209**, 108648 (2021).
[30]F. Arpino, G. Grossi, G. Cortellessa, A. Mikszewski, L. Morawska, G. Buonanno, and L. Stabile, "Risk of SARS-CoV-2 in a car cabin assessed through 3D CFD simulations," Indoor Air **32**(3), e13012 (2022).
[31]T.-B. Chang, J.-J. Sheu, J.-W. Huang, Y.-S. Lin, and C.-C. Chang, "Development of a CFD model for simulating vehicle cabin indoor air quality," Transp. Res. Part D **62**, 433–440 (2018).
[32]C.-J. Yang, T.-C. Yang, P.-T. Chen, and K. D. Huang, "An innovative design of regional air conditioning to increase automobile cabin energy efficiency," Energies **12**(12), 2352 (2019).
[33]S. Khatoon and M.-H. Kim, "Thermal comfort in the passenger compartment using a 3-D numerical analysis and comparison with Fanger's comfort models," Energies **13**(3), 690 (2020).
[34]H. Zhang, L. Dai, G. Xu, Y. Li, W. Chen, and W.-Q. Tao, "Studies of air-flow and temperature fields inside a passenger compartment for improving thermal comfort and saving energy. Part I: Test/numerical model and validation," Appl. Therm. Eng. **29**(10), 2022–2027 (2009).
[35]H. Zhang, L. Dai, G. Xu, Y. Li, W. Chen, and W. Tao, "Studies of air-flow and temperature fields inside a passenger compartment for improving thermal comfort and saving energy. Part II: Simulation results and discussion," Appl. Therm. Eng. **29**(10), 2028–2036 (2009).
[36]T. Dehne, P. Lange, A. Volkmann, D. Schmeling, M. Konstantinov, and J. Bosbach, "Vertical ventilation concepts for future passenger cars," Build. Environ. **129**, 142–153 (2018).
[37]S. Ullrich, R. Buder, N. Boughanmi, C. Friebe, and C. Wagner, *New Results in Numerical and Experimental Fluid Mechanics XII*, edited by A. Dillmann, G. Heller, E. Krämer, C. Wagner, C. Tropea, and S. Jakirlić (Springer International Publishing, Cham, 2020), pp. 457–467.
[38]M. Djeddou, A. Mehel, G. Fokoua, A. Tanière, and P. Chevrier, "On the application of statistical turbulence models to the simulation of airflow inside a car cabin," Phys. Fluids **35**(2), 025106 (2023).
[39]V. Mathai, A. Das, and K. Breuer, "Aerosol transmission in passenger car cabins: Effects of ventilation configuration and driving speed," Phys. Fluids **34**(2), 021904 (2022).
[40]N. Sen and K. K. Singh, "Spread of virus laden aerosols inside a moving sports utility vehicle with open windows: A numerical study," Phys. Fluids **33**(9), 095117 (2021).
[41]P. Dancă, A. Jamin, I. Nastase, B. Janssens, W. Bosschaerts, and C. Coșoiu, "Experimental and numerical study of the flow dynamics and thermal behavior inside a car cabin: Innovative air diffusers and human body plumes interactions," Energy Rep. **8**, 992–1002 (2022).
[42]P. A. Danca, I. Nastase, and F. Bode, "The influence of different air flows introduced on the thermal comfort of car passengers during the cooling period—Numerical Study," IOP Conf. Ser. **664**(1), 012112 (2021).
[43]M. Djeddou, A. Mehel, G. Fokoua, A. Tanière, and P. Chevrier, "A Diffusion-Inertia Model for the simulation of particulate pollutants dynamics inside a car cabin," J. Aerosol Sci. **175**, 106279 (2024).
[44]Y. Pan, W. Huang, H. K. Dai, Y. Bian, K.-F. Ho, and C. Chen, "Evaluation of intervention measures in reducing the driver's exposure to respiratory particles in a taxi with infected passengers," Sci. Total Environ. **902**, 166099 (2023).
[45]P. Bandi, N. P. Manelil, M. P. Maiya, S. Tiwari, and T. Arunvel, "CFD driven prediction of mean radiant temperature inside an automobile cabin using machine learning," Therm. Sci. Eng. Prog. **37**, 101619 (2023).
[46]A. Sciacchitano, F. Arpino, and G. Cortellessa, "Benchmark PIV database for the validation of CFD simulations in a transitional cavity flow," Int. J. Heat Fluid Flow **90**, 108831 (2021).
[47]J. Sip, F. Lizal, J. Pokorny, J. Elcner, J. Jedelsky, and M. Jicha, "Automotive cabin vent: Comparison of RANS and LES approaches with analytical-empirical equations and their validation with experiments using hot-wire anemometry," Build. Environ. **233**, 110072 (2023).
[48]ISO, *ISO 7730:2005—Ergonomics of the Thermal Environment—Analytical Determination and Interpretation of Thermal Comfort using Calculation of the PMV and PPD Indices and Local Thermal Comfort Criteria* (ISO, 2005).
[49]ANSI, *ANSI/ASHRAE Standard 55–2020: Thermal Environmental Conditions for Human Occupancy* (ANSI, 2020).
[50]T. Ležovič, F. Lízal, J. Jedelský, and M. Jícha, "HVAC automotive vents evaluation and their performance," HVACR Res. **19**(8), 1073–1082 (2013).
[51]M. Bertone, A. Sciacchitano, F. Arpino, C. Canale, G. Cortellessa, G. Grossi, and L. Moretti, "Experimental characterization of the airflow within a car cabin," J. Phys.: Conf. Ser. **2509**(1), 012024 (2023).
[52]I. Golasi, F. Salata, E. de Lieto Vollaro, M. Coppi, and A. de Lieto Vollaro, "Thermal perception in the Mediterranean area: Comparing the Mediterranean outdoor comfort index (MOCI) to other outdoor thermal comfort indices," Energies **9**(7), 550 (2016).
[53]A. Alahmer, A. Mayyas, A. A. Mayyas, M. A. Omar, and D. Shan, "Vehicular thermal comfort models; a comprehensive review," Appl. Therm. Eng. **31**(6–7), 995–1002 (2011).
[54]P. Danca, A. Vartires, and A. Dogeanu, "An overview of current methods for thermal comfort assessment in vehicle cabin," Energy Proc. **85**, 162–169 (2016).
[55]P. Danca, I. Nastase, F. Bode, C. Croitoru, A. Dogeanu, and A. Meslem, "Evaluation of the thermal comfort for its occupants inside a vehicle during summer," IOP Conf. Ser. **595**, 012027 (2019).
[56]I. Nastase, P. Danca, F. Bode, C. Croitoru, L. Fechete, M. Sandu, and C. I. Coșoiu, "A regard on the thermal comfort theories from the standpoint of electric vehicle design—Review and perspectives," Energy Rep. **8**, 10501–10517 (2022).
[57]ISO, *ISO/TS 14505-1:2007. Ergonomics of the Thermal Environment—Evaluation of Thermal Environments in Vehicles—Part 1: Principles and Methods for Assessment of Thermal Stress* (ISO, 2007).
[58]F. Tartarini and S. Schiavon, "pythermalcomfort: A Python package for thermal comfort research," SoftwareX **12**, 100578 (2020).
[59]D. Khovalyg, O. B. Kazanci, H. Halvorsen, I. Gundlach, W. P. Bahnfleth, J. Toftum, and B. W. Olesen, "Critical review of standards for indoor thermal environment and air quality," Energy Build. **213**, 109819 (2020).
[60]J. H. Ferziger and M. Perić, *Computational Methods for Fluid Dynamics*, 3rd ed. (Springer, Berlin, Heidelberg, 2002).
[61]P. J. Roache, "Quantification of uncertainty in computational fluid dynamics," Annu. Rev. Fluid Mech. **29**(1), 123–160 (1997).
[62]F. Nicoud and F. Ducros, "Subgrid-scale stress modelling based on the square of the velocity gradient tensor," Flow, Turbul. Combust. **62**(3), 183–200 (1999).
[63]W.-W. Kim and S. Menon, "A new dynamic one-equation subgrid-scale model for large eddy simulations," AIAA Paper No. 1995-356, 1995.
[64]I. B. Celik, Z. N. Cehreli, and I. Yavuz, "Index of resolution quality for large eddy simulations," J. Fluids Eng. **127**(5), 949–958 (2005).
[65]S. B. Pope, *Turbulent Flows*, 1st ed. (Cambridge University Press, 2000).

[66]R. Poletto, T. Craft, and A. Revell, "A new divergence free synthetic eddy method for the reproduction of inlet flow conditions for LES," Flow. Turbul. Combust. **91**(3), 519–539 (2013).
[67]M. Shur, M. Strelets, A. Travin, A. Probst, S. Probst, D. Schwamborn, S. Deck, A. Skillen, J. Holgate, A. Revell, C. W, and D. Schwamborn, *Go4Hybrid: Grey Area Mitigation for Hybrid RANS-LES Methods*, edited by C. Mockett and W. Haase (Springer International Publishing, Cham, 2018), pp. 51–87.
[68]K. Gładyszewska-Fiedoruk and T. J. Teleszewski, "Modeling of humidity in passenger cars equipped with mechanical ventilation," Energies **13**(11), 2987 (2020).